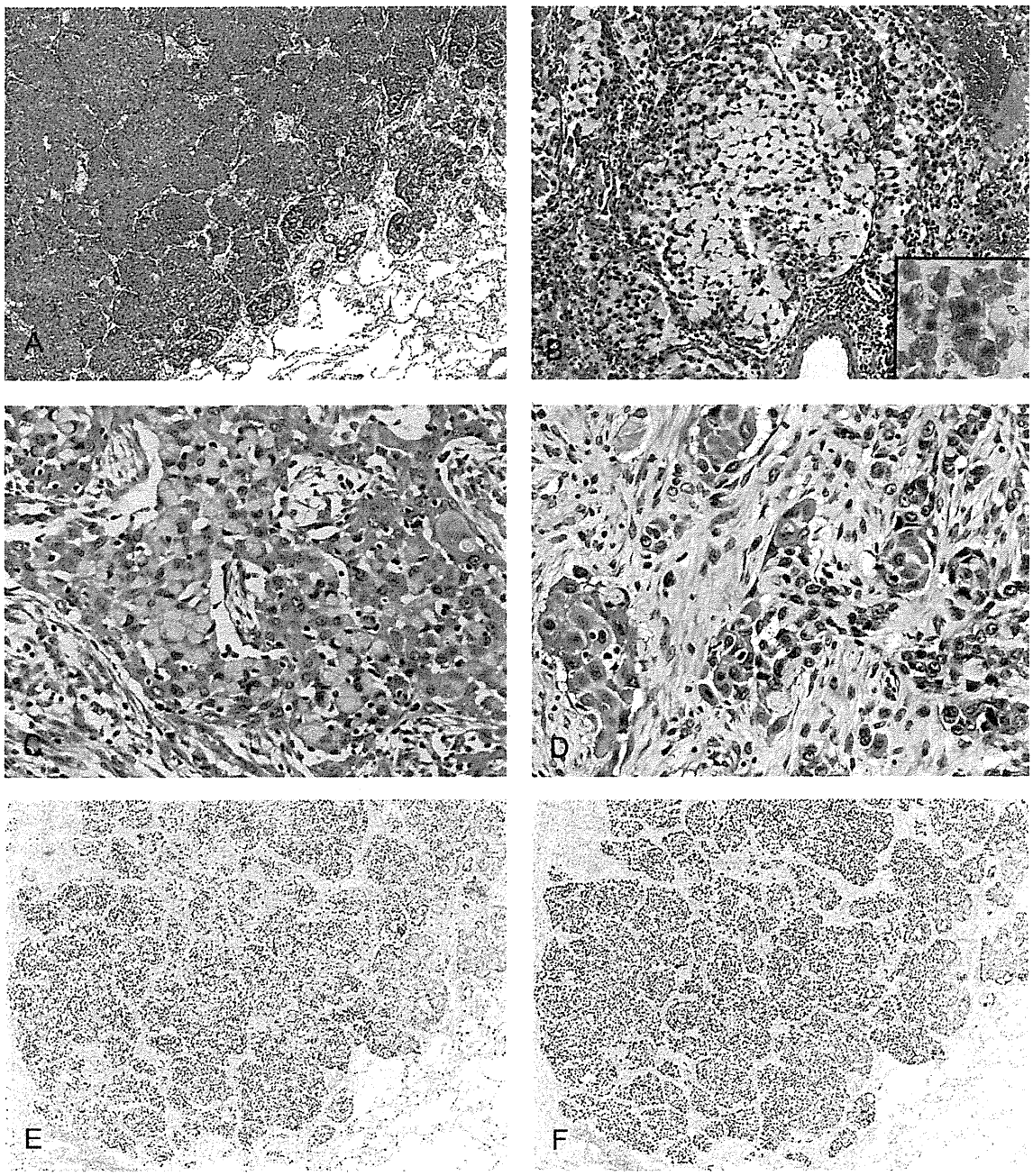

Fig. 1. Histological features of Ad-SRCCs of the lung showing solid/acinar growth with an alveolar filling pattern at the lesion periphery (A, H&E, case 1). Signet-ring cells were present at the center of a large tumor cell nest. Notice characteristic cohesive clustering of signet-ring cells and relatively monomorphic nuclei. Intracytoplasmic mucin in signet-ring cells was highlighted dark blue by alcian blue-periodic acid-Schiff (AB-PAS) staining, shown in the inset (B, H&E, case 6; inset, AB-PAS). Clusters of signet-ring cells in smaller nests (C, H&E, case 7). One tumor harboring the *EML4-ALK* fusion gene showed focal squamous differentiation (D, H&E, case 10). Fifty percent of Ad-SRCCs diffusely co-expressed TTF-1 (E, TTF-1 immunostain, case 1) and p63 (F, p63 immunostain, case 1).

3. Results

3.1. Clinicopathological features

Ten (1.4%) cases of lung Ad-SRCC were identified out of 699 consecutive primary adenocarcinomas resected at NCC Tokyo (2004–2005). The pertinent clinicopathological data are summarized in Table 2, along with the immunohistochemical and genetic results. The patients were five men and five women with a mean age of 58 (range, 33–78) years. They were slightly younger than 699 primary lung adenocarcinoma patients treated during the study period (mean age 63.4 years old, $p = 0.038$). There were five non-smokers, two light smokers (<20 pack-years), and three heavy smokers (≥20 pack-years). The tumors all appeared well circumscribed on gross examination and measured 2.7 cm in diameter on average (range, 1.0–5.0 cm). Five tumors were found at stage I, one was at stage II, and three were at stage III. Histologically, all the tumors contained, by definition, at least 5% signet-ring cells. AB-PAS staining highlighted mucin as dark blue spherules in all cases (Fig. 1B, inset). The ratio of signet-ring cells relative to the total tumor cells varied with an average of 13% (range, 5–30%). In all cases, the signet-ring cells formed tight or loose cohesive

Table 2
Clinicopathological findings, and *EGFR*, *KRAS*, and *ALK* status of the present 10 Ad-SRCCs of the lung.

Case #	Age	Sex	SI	Size (cm)	Stage	Follow-up, months	WHO predominant pattern	SRC%	Nuclear grade	TTF-1 IHC	p63 IHC	*ALK* RT-PCR	*ALK* FISH	ALK IHC	*EGFR*	*KRAS*
1	34	F	14	1.8	IA	NED, 60	Solid	20	Low	3+	3+	+	+[a]	+	WT	WT
2	60	M	29	1.8	IA	NED, 64	Acinar	5	Low	3+	3+	–	NA	–	WT	WT
3	56	F	0	4.5	IIIA	DOD, 32	Solid	5	Low	3+	1+	–	–	–	WT	WT
4	63	M	30	5.0	IIIA	AWD, 3	Acinar	5	Intermediate	3+	1+	–	Ind	–	WT	WT
5	78	M	10	3.0	IA	AWD, 53	Solid	5	Intermediate	0	0	–	–	–	WT	WT
6	63	F	0	3.0	IIIB	NED, 50	Solid	20	Low	3+	3+	–	–	–	WT	WT
7	68	M	30	2.5	IIA	NED, 51	Solid	5	Intermediate	2+	2+	–	+	–	WT	WT
8	77	F	0	2.5	IA	NED, 48	Papillary	15	Low	3+	2+	+	Ind	+	WT	WT
9	51	M	0	1.0	IIIA	NED, 47	Solid	20	Low	3+	3+	+	+	+	WT	WT
10	33	F	0	1.4	IB	NED, 62	Solid	30	Intermediate	3+	3+	NA	+[a]	+	WT	WT

F, female; M, male; SI, smoking index (number of packs of cigarettes per day × years); NED, no evidence of disease; DOD, died of disease; AWD, alive with disease; SRC%, percentage of signet-ring cells; NA, not available; Ind, indeterminate; WT, wild type.
[a] Cases showing a single orange signal and one fused signal on FISH.

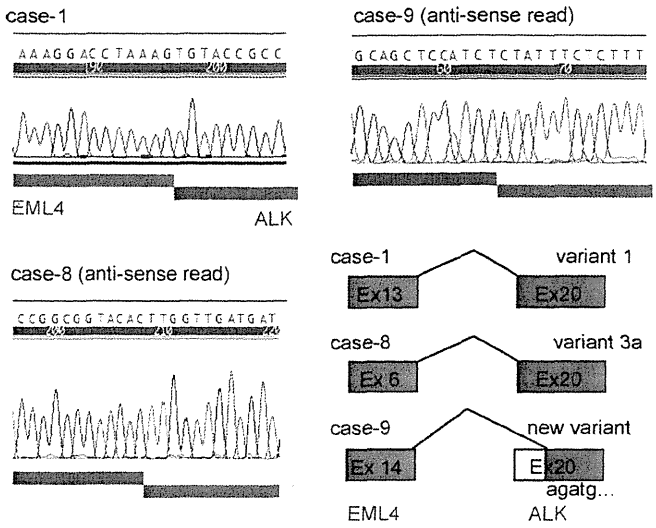

Fig. 2. RT-PCR and sequence analysis identified the presence of *EML4-ALK* fusion transcripts in three cases (cases 1, 8, and 9) of Ad-SRCC.

clusters within solid nests of tumor cells (Fig. 1B and C), typically appearing in the central portion of nests. The tumor cell nests filled and expanded the alveolar spaces at the lesional periphery in nine cases (Fig. 1A). The tumor cell nuclei were relatively monomorphic, except for focal areas of pleomorphism in case 4, and showed low- (six cases) to intermediate-grade (four cases) atypism. The predominant WHO growth pattern was solid in seven cases, acinar in two, and papillary in one. Signet-ring cells were associated with a solid pattern in eight cases, an acinar pattern in one, and both acinar and solid patterns in one. Lepidic growth was absent in all the cases except for case 6. One tumor (case 10) showed focal squamous differentiation (Fig. 1D). Extracellular mucin was minimal in all cases. Nine Ad-SRCCs were diffusely immunopositive for TTF-1 (Fig. 1E). Nine tumors were also immunoreactive for p63, and five of them showed diffuse (>50%) labeling with strong intensity (Fig. 1F). In seven cases, the foci of signet-ring cells within the tumor co-expressed TTF-1 and p63 (cases 1, 2, 6–10). Follow-up information was available for all of the patients. Seven patients were alive and well without recurrence after a mean follow-up period of 55 months (range, 47–64 months), two patients were alive with distant recurrence at 3 and 53 months, respectively. The remaining patient died of the disease 32 months after surgery.

3.2. *ALK* analysis (RT-PCR, FISH, and IHC)

The expected PCR products of the *EML4-ALK* fusion gene were observed in three out of nine tested cases, and none of the *KIF5B-ALK* fusion transcripts was amplified. The sequence of each PCR product revealed that these three cases had different fusion transcripts (Fig. 2). The detected transcripts were variant 1 in case 1 and variant 3a in case 8. Case 9 harbored a new breakpoint connecting *EML4* exon 14 and the 12-amino-acids-deleted *ALK* exon 20.

Among the three RT-PCR-proven ALK-translocated cases, unanimous agreement on the positive *ALK* rearrangement was obtained for two tumors by FISH (Fig. 3). The remaining case (case 8) was designated as indeterminate for *ALK* rearrangement, and it showed more than 2 pairs of signals in the vast majority of the tumor cells, the significance of which finding was unclear. Among the six PCR-negative cases, FISH was unsuccessful in one case, three were designated as negative, one was designated as indeterminate, and one was designated as positive for *ALK* rearrangement. The latter case (case 7) showed a small number of tumor cells exhibiting wider split signals than expected for *EML4-ALK* fusion. Case 10, whose

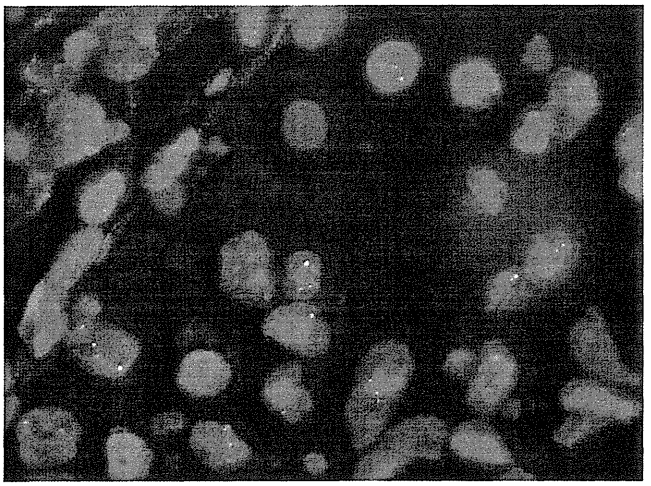

Fig. 3. FISH study using an *ALK* break-apart probe showed *ALK* rearrangement (splitting of green and orange signals) in an Ad-SRCC (case 9).

fresh tissue was not available for RT-PCR analysis, was shown to be positive for *ALK* rearrangement by FISH. In cases 1 and 10, more than 50% of the counted 100 tumor cells demonstrated loss of 5′ locus of split-apart *ALK*, showing one fused signal and one orange signal per cell.

The results of IHC were in accordance with those of PCR. All of the three PCR-positive tumors were strongly reactive for ALK antibody (Fig. 4), and all of the six PCR-negative tumors were non-reactive for this marker. Case 10, in which *ALK* rearrangement was detected by FISH, also showed strong labeling for ALK antibody.

3.3. *EGFR and KRAS mutation analyses*

No mutation of the *EGFR* or *KRAS* gene was detected by sequencing in the nine studied cases. Case 10 was also negative for *EGFR* or *KRAS* mutation by high-resolution mutation analysis.

4. Discussion

The clinical and histological findings in the present series were generally in accord with prior reports. The incidence of Ad-SRCCs in this series was 1.4%, in keeping with the rarity (0.14–1.9%) reported by other authors [21–23,26]. Younger age at onset and light tobacco exposure in the present series also concurred with the findings of other studies [21–24,32]. Unlike others [22,23,27], however, the majority of the tumors in this series had a lower stage (I or II) at presentation, and their prognoses were accordingly fair, but these findings likely reflect that all of our cases were surgically resected at the institution which treats many small-sized lung tumors. Besides their defining cytological attribute, Ad-SRCCs showed characteristic architectural profiles as described previously [21,24,27], including solid nests, cohesive clustering of signet-ring cells, and alveolar filling patterns at the lesional periphery [21,23,33]. The cohesiveness of signet-ring cells is somewhat at variance with most homonymous tumors in the stomach or breast, which often infiltrate diffusely as isolated cells. The nuclei of the Ad-SRCCs in this series were uniform and of low to intermediate grade without frank anaplasia in most cases, though the nuclear features of Ad-SRCCs have not been fully analyzed in the past [23].

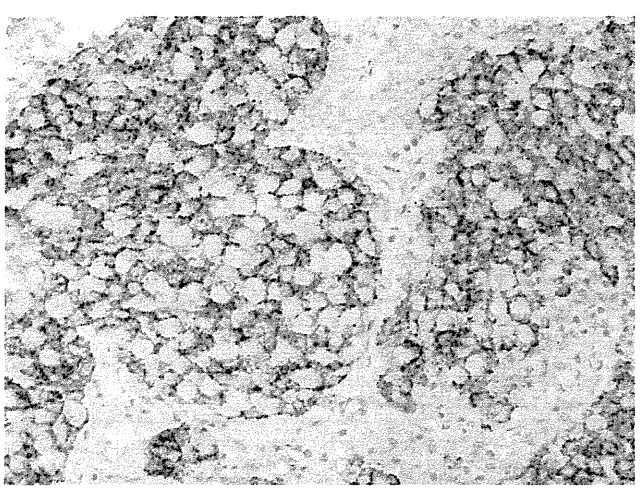

Fig. 4. ALK protein is immunohistochemically positive in an Ad-SRCC (ALK immunostain, case 1).

Immunohistochemically, most of our Ad-SRCCs were positive for TTF-1, as expected [23,26]. Interestingly, most tumors also labeled for p63, and half were stained in diffuse strong manner by this antibody. The immunoreactivity of p63 in lung adenocarcinomas is considered to be uncommon [34,35], and a recent report in abstract form [36] showed that significant co-expression of TTF-1 and p63 occurred in only 5.5% of adenocarcinomas of the lung in general. This previously unrecognized peculiar immunoprofile of Ad-SRCC may indicate that this tumor subtype might arise from a specific cell of origin, different from most lung adenocarcinomas. Although diffuse strong p63 positivity is often used as a marker of squamous cell carcinoma in diagnostic pathology, Ad-SRCC seems a major pitfall to this practice. Careful attention to the focal signet-ring cell element and TTF-1 staining should lead to the correct diagnosis.

Since ALK analysis was partly complicated by the technical difficulty of FISH (see below), we required evidence of *ALK* alteration on the basis of at least two different modalities for the diagnosis of *ALK*-translocated cancer. Four of the 10 cases (40%) of lung Ad-SRCC were thus regarded as positive for *ALK* rearrangements (cases 1, 8, 9, and 10). This result is in accord with Rodig et al. [11], who found that 14 of 47 (30%) Ad-SRCCs showed *ALK* rearrangement by FISH. *ALK*-rearranged tumors in this study had a significantly more proportion of signet-ring cell components than *ALK* wild-type tumors (mean 44% vs. 10%; $p = 0.0058$), and this trend was also in agreement with the previous report [11]. Although it was suspected that the presence of signet-ring cell in *ALK*-rearranged tumors might be a regionally/ethnically limited phenomenon [11], we showed that it is rather a universal finding also evident in non-Western patients.

Because the *EML4-ALK* fusion in lung cancer is rare (3.8%) [17] in unselected populations, and because the currently accepted methods for detecting this chimeric gene are relatively expensive and labor-intensive, a practical concentration strategy is needed for effectively preselecting a subgroup of patients whose tumors are more likely to be positive for *ALK* translocation [2]. The present study used histological criteria alone, i.e. those of Ad-SRCC, to successfully extract a subset of adenocarcinomas carrying *ALK* translocation in as many as 40% of the cases. Other clinical (e.g., younger age and minimal tobacco exposure) and histological (e.g., solid or acinar pattern) features known to be associated with *ALK*-rearranged tumors [8,12] may also be used in combination with the signet-ring cells in order to enhance the detection rate. Rodig et al. [11] indeed noted that as many as 50% of their tumors showing a combination of solid growth and the presence of >10% signet-ring cells harbored *ALK* rearrangement.

The minor discordance of *ALK* status among the modalities used in this study resulted primarily from FISH analysis, whereas the results of RT-PCR and IHC were completely concordant. Interpretation of FISH results for *EML4-ALK*-positive lung cancer is known to

be technically difficult [2,11]. Because both the *EML4* and *ALK* genes are located close to each other on the same chromosome arm, their fusion yields a split signal separated by only a short distance. Consequently, identifying a split is not as straightforward as in other translocation-associated tumors, and the criteria for recognition of positive split signals may vary among observers. Such variability may well have contributed to the present FISH results, for which opinions on two cases conflicted among different observers. One case (case 7) was interpreted as FISH-positive, as opposed to the results of RT-PCR and IHC. That tumor contained a small number of cells with *ALK*-split signals showing a much wider distance than would be expected for *EML4-ALK* fusion. The RT-PCR study of the kinase domain of *ALK* in this case showed no expression of the *ALK* gene, virtually ruling out any unknown functional translocation involving *ALK* (data not shown), and the significance of this FISH result is unclear. Although some previous studies using FISH assay with commercially available probes appeared to yield results that were more concordant with RT-PCR or IHC [6,11], our data call attention to the inherent difficulty attached to this modality, and emphasize the need for caution when integrating FISH into routine diagnostics for *ALK*-rearranged lung cancer. The development of smaller customized probes may be helpful for more reliable detection of this genetic change.

The *EML4-ALK* fusion gene detected in patient 9 in the present series is a novel variant, in which *EML4* exon 14 was joined with part of exon 20 at a point 36 nucleotides distal to the beginning of exon 20 of *ALK*. This transcript would be read in-frame to generate an intact chimeric protein that maintains the kinase domain of the *ALK* gene, and would be expected to result in overactivation of the signaling pathway downstream to ALK. The literature regarding the nomenclature of the *EML4-ALK* variants is somewhat confusing; seven variants (1, 2, 3a, 3b, 4, 5a, 5b, 6, and 7) were discovered by the same group of investigators, while two different groups have independently identified variants "4" and "5", respectively [2]. Recently, two more variants were added [14], and thus, to our knowledge, the current variant is the 12th. There are no conclusive data to indicate whether different variants are associated with different clinical or histological features.

One of the tumors shown to be positive for ALK alteration by FISH and IHC exhibited focal squamous differentiation. Although most of the previous reports have documented the exclusive adenocarcinoma histology of *ALK*-rearranged tumors, a small number have been reported to show squamous differentiation [5,6,11,16]. The current additional case further reinforces the view that the presence of *EML4-ALK* fusion is not restricted to a pure adenocarcinoma histology. Wong et al. [16] have even identified an *EML4-ALK* fusion gene in a tumor that was interpreted as mucoepidermoid carcinoma. Notably, the combination of solid growth, uniform lower-grade nuclei, clusters of mucin-rich cells, frequent diffuse p63 immunoreactivity, and rare unequivocal squamous differentiation seen in our present series of Ad-SRCCs imparted a superficial resemblance to mucoepidermoid carcinoma. However, a coexisting typical acinar or papillary growth pattern of adenocarcinoma, lack of endobronchial growth, and TTF-1 immunopositivity readily ruled out that possibility. *CRTC1-MAML2* or *CRTC3-MAML2* translocations associated with mucoepidermoid carcinomas [37] were not identified by RT-PCR in any of the present Ad-SRCCs (cases 1–9) (data not shown).

ALK-translocation-positive Ad-SRCCs in this series lacked mutations of either *EGFR* or *KRAS*, confirming the prior observations that *ALK* alteration is mutually exclusive of such genetic events [5,8,9,12,13,16]. What is particularly interesting here is that there was also a total absence of *EGFR* and *KRAS* mutations in the Ad-SRCCs without *ALK* translocations. Considering the high frequency (up to 71% [32]) of *EGFR* or *KRAS* mutations of lung adenocarcinomas in the Japanese population, our findings appear to suggest the unique genetic background of Ad-SRCC of the lung, despite the admittedly small number of cases studied. It is possible that a certain pathway downstream to the EML4-ALK chimeric protein plays a critical role in creation of the signet-ring cell morphology, and the same pathway may function even in Ad-SRCCs without *ALK* fusion genes. Alternatively, Ad-SRCCs may originate from a certain type of cell that is programmed to differentiate to a signet-ring cell phenotype, and such cells may be somehow more prone to accumulate *ALK* alterations than *EGFR* or *KRAS* mutations. It is unlikely that *EML4-ALK* itself determines the signet-ring cell cytology, because not all of the *ALK*-translocation-positive adenocarcinomas of the lung showed this particular cell type [11]. It is noteworthy that certain clinical features (younger age at onset and minimal tobacco exposure) are shared by both Ad-SRCCs and *ALK*-rearranged tumors [8,12,21,22], possibly suggesting an inherent close relationship between the two. A few previous reports have detected *KRAS* mutations in some Ad-SRCCs [24,26], and this discrepancy may be due to the small number of cases examined, or differences in the criteria used to select the Ad-SRCCs.

In conclusion, this study has confirmed the previously observed association between Ad-SRCC and *ALK*-rearrangement. The characteristic histology, immunoprofile (TTF-1/p63 co-expression), frequent *ALK* translocation, and total lack of *EGFR* or *KRAS* mutations, may suggest that Ad-SRCC forms a coherent subgroup of lung adenocarcinomas.

Conflict of interest

None declared.

Acknowledgements

The authors thank Drs. H. Mano and M. Soda for providing us information about the sequence of primers and multiplex PCR condition. We also thank Ms. Karin Yokozawa, Mr. Susumu Wakai, Ms. Sachiko Miura, and Ms. Chizu Kina for superb technical assistance. This work was supported in part by Grant-in-Aid for Cancer Research from the Ministry of Health, Labor and Welfare of Japan (T.S.), and by Grant-in-Aid for the Third-Term Comprehensive 10-Year Strategy for Cancer Control from the Ministry of Health, Labor and Welfare of Japan (H.T.).

References

[1] Travis WD, Brambilla E, Muller-Hermelink HK, Harris CC. Pathology and genetics: tumours of the lung, pleura, thymus and heart. Lyon, France: IARC Press; 2004.
[2] Horn L, Pao W. EML4-ALK: honing in on a new target in non-small-cell lung cancer. J Clin Oncol 2009;27:4232–5.
[3] Lynch TJ, Bell DW, Sordella R, Gurubhagavatula S, Okimoto RA, Brannigan BW, et al. Activating mutations in the epidermal growth factor receptor underlying responsiveness of non-small-cell lung cancer to gefitinib. N Engl J Med 2004;350:2129–39.
[4] Paez JG, Janne PA, Lee JC, Tracy S, Greulich H, Gabriel S, et al. EGFR mutations in lung cancer: correlation with clinical response to gefitinib therapy. Science 2004;304:1497–500.
[5] Soda M, Choi YL, Enomoto M, Takada S, Yamashita Y, Ishikawa S, et al. Identification of the transforming EML4-ALK fusion gene in non-small-cell lung cancer. Nature 2007;448:561–6.
[6] Boland JM, Erdogan S, Vasmatzis G, Yang P, Tillmans LS, Erickson Johnson MR, et al. Anaplastic lymphoma kinase immunoreactivity correlates with ALK gene rearrangement and transcriptional up-regulation in non-small cell lung carcinomas. Hum Pathol 2009;40:1152–8.
[7] Choi YL, Takeuchi K, Soda M, Inamura K, Togashi Y, Hatano S, et al. Identification of novel isoforms of the EML4-ALK transforming gene in non-small cell lung cancer. Cancer Res 2008;68:4971–6.
[8] Inamura K, Takeuchi K, Togashi Y, Hatano S, Ninomiya H, Motoi N, et al. EML4-ALK lung cancers are characterized by rare other mutations, a TTF-1 cell lineage, an acinar histology, and young onset. Mod Pathol 2009;22:508–15.
[9] Inamura K, Takeuchi K, Togashi Y, Nomura K, Ninomiya H, Okui M, et al. EML4-ALK fusion is linked to histological characteristics in a subset of lung cancers. J Thorac Oncol 2008;3:13–7.

[10] Koivunen JP, Mermel C, Zejnullahu K, Murphy C, Lifshits E, Holmes AJ, et al. EML4-ALK fusion gene and efficacy of an ALK kinase inhibitor in lung cancer. Clin Cancer Res 2008;14:4275–83.
[11] Rodig SJ, Mino-Kenudson M, Dacic S, Yeap BY, Shaw A, Barletta JA, et al. Unique clinicopathologic features characterize ALK-rearranged lung adenocarcinoma in the western population. Clin Cancer Res 2009;15:5216–23.
[12] Shaw AT, Yeap BY, Mino-Kenudson M, Digumarthy SR, Costa DB, Heist RS, et al. Clinical features and outcome of patients with non-small-cell lung cancer who harbor EML4-ALK. J Clin Oncol 2009;27:4247–53.
[13] Shinmura K, Kageyama S, Tao H, Bunai T, Suzuki M, Kamo T, et al. EML4-ALK fusion transcripts, but no NPM-, TPM3-, CLTC-, ATIC-, or TFG-ALK fusion transcripts, in non-small cell lung carcinomas. Lung Cancer 2008;61:163–9.
[14] Takahashi T, Sonobe M, Kobayashi M, Yoshizawa A, Menju T, Nakayama E, et al. Clinicopathologic features of non-small-cell lung cancer with EML4-ALK fusion gene. Ann Surg Oncol 2010;17:889–97.
[15] Takeuchi K, Choi YL, Togashi Y, Soda M, Hatano S, Inamura K, et al. KIF5B-ALK, a novel fusion oncokinase identified by an immunohistochemistry-based diagnostic system for ALK-positive lung cancer. Clin Cancer Res 2009;15:3143–9.
[16] Wong DW, Leung EL, So KK, Tam IY, Sihoe AD, Cheng L, et al. The EML4-ALK fusion gene is involved in various histologic types of lung cancers from nonsmokers with wild-type EGFR and KRAS. Cancer 2009;115:1723–33.
[17] Solomon B, Varella-Garcia M, Camidge DR. ALK gene rearrangements: a new therapeutic target in a molecularly defined subset of non-small cell lung cancer. J Thorac Oncol 2009;4:1450–4.
[18] Soda M, Takada S, Takeuchi K, Choi YL, Enomoto M, Ueno T, et al. A mouse model for EML4-ALK-positive lung cancer. Proc Natl Acad Sci USA 2008;105:19893–7.
[19] Kwak EL, Camidge DR. Clinical activity observed in a phase I dose escalation trial of an oral c-met and ALK inhibitor, PF-02341966. J Clin Oncol 2009:27.
[20] Kish JK, Ro JY, Ayala AG, McMurtrey MJ. Primary mucinous adenocarcinoma of the lung with signet-ring cells: a histochemical comparison with signet-ring cell carcinomas of other sites. Hum Pathol 1989;20:1097–102.
[21] Tsuta K, Ishii G, Yoh K, Nitadori J, Hasebe T, Nishiwaki Y, et al. Primary lung carcinoma with signet-ring cell carcinoma components: clinicopathological analysis of 39 cases. Am J Surg Pathol 2004;28:868–74.
[22] Ou SH, Ziogas A, Zell JA. Primary signet-ring carcinoma (SRC) of the lung: a population-based epidemiologic study of 262 cases with comparison to adenocarcinoma of the lung. J Thorac Oncol 2010;5:420–7.
[23] Castro CY, Moran CA, Flieder DG, Suster S. Primary signet ring cell adenocarcinomas of the lung: a clinicopathological study of 15 cases. Histopathology 2001;39:397–401.
[24] Hayashi H, Kitamura H, Nakatani Y, Inayama Y, Ito T, Kitamura H. Primary signet-ring cell carcinoma of the lung: histochemical and immunohistochemical characterization. Hum Pathol 1999;30:378–83.
[25] Merchant SH, Amin MB, Tamboli P, Ro J, Ordonez NG, Ayala AG, et al. Primary signet-ring cell carcinoma of lung: immunohistochemical study and comparison with non-pulmonary signet-ring cell carcinomas. Am J Surg Pathol 2001;25:1515–9.
[26] Maeshima A, Miyagi A, Hirai T, Nakajima T. Mucin-producing adenocarcinoma of the lung, with special reference to goblet cell type adenocarcinoma: immunohistochemical observation and Ki-ras gene mutation. Pathol Int 1997;47:454–60.
[27] Iwasaki T, Ohta M, Lefor AT, Kawahara K. Signet-ring cell carcinoma component in primary lung adenocarcinoma: potential prognostic factor. Histopathology 2008;52:639–40.
[28] Tsuta K, Ishii G, Nitadori J, Murata Y, Kodama T, Nagai K, et al. Comparison of the immunophenotypes of signet-ring cell carcinoma, solid adenocarcinoma with mucin production, and mucinous bronchioloalveolar carcinoma of the lung characterized by the presence of cytoplasmic mucin. J Pathol 2006;209:78–87.
[29] Sobin LH, Wittekind C, editors. International Union Against Cancer (UICC) TNM classification of malignant tumours. 6th ed. New York: Wiley-Liss; 2002.
[30] Paik J, Choe J, Chung J. Protein expression and gene rearrangement of ALK in non-small cell lung carcinomas. Mod Pathol 2010;23:411A.
[31] Fukui T, Ohe Y, Tsuta K, Furuta K, Sakamoto H, Takano T, et al. Prospective study of the accuracy of EGFR mutational analysis by high-resolution melting analysis in small samples obtained from patients with non-small cell lung cancer. Clin Cancer Res 2008;14:4751–7.
[32] Sakuma Y, Matsukuma S, Yoshihara M, Nakamura Y, Noda K, Nakayama H, et al. Distinctive evaluation of nonmucinous and mucinous subtypes of bronchioloalveolar carcinomas in EGFR and K-ras gene-mutation analyses for Japanese lung adenocarcinomas: confirmation of the correlations with histologic subtypes and gene mutations. Am J Clin Pathol 2007;128:100–8.
[33] Sarma DP, Hoffmann EO. Primary signet-ring cell carcinoma of the lung. Hum Pathol 1990;21:459–60.
[34] Sheikh HA, Fuhrer K, Cieply K, Yousem S. p63 expression in assessment of bronchioloalveolar proliferation of the lung. Mod Pathol 2004;17:1134–40.
[35] Wu M, Orta L, Gil J, Li G, Hu A, Burstein DE. Immunohistochemical detection of XIAP and p63 in adenomatous hyperplasia, atypical adenomatous hyperplasia, bronchioloalveolar carcinoma and well-differentiated adenocarcinoma. Mod Pathol 2008;21:553–8.
[36] Ang D, Ghaffar H, Zakowski M, Teruya-Feldstein J, Moreira A, Rekhtman N. Expression of squamous markers in lung adenocarcinoma: clinicopathologic and molecular correlates, and implications for differentiation from squamous cell carcinoma. Mod Pathol 2010;23:397A.
[37] Nakayama T, Miyabe S, Okabe M, Sakuma H, Ijichi K, Hasegawa Y, et al. Clinicopathological significance of the CRTC3-MAML2 fusion transcript in mucoepidermoid carcinoma. Mod Pathol 2009;22:1575–81.

Lung Cancer 70 (2010) 286–294

Contents lists available at ScienceDirect

Lung Cancer

journal homepage: www.elsevier.com/locate/lungcan

Automated assessment of malignant degree of small peripheral adenocarcinomas using volumetric CT data: Correlation with pathologic prognostic factors

Masahiro Yanagawa[a,*], Yuko Tanaka[a], Masahiko Kusumoto[b], Shunichi Watanabe[c], Ryosuke Tsuchiya[d], Osamu Honda[a], Hiromitsu Sumikawa[a], Atsuo Inoue[a], Masayoshi Inoue[d], Meinoshin Okumura[d], Noriyuki Tomiyama[a], Takeshi Johkoh[e]

[a] Department of Radiology, Osaka University Graduate School of Medicine, 2-2 Yamadaoka, Suita-city, Osaka 565-0871, Japan
[b] Department of Radiology, National Cancer Center, 5-1-1 Tukiji, Chuo-ku, Tokyo 104-0045, Japan
[c] Division of Thoracic Surgery, National Cancer Center, 5-1-1 Tukiji, Chuo-ku, Tokyo 104-0045, Japan
[d] Respiratory Surgery, Osaka University Graduate School of Medicine, 2-2 Yamadaoka, Suita-city, Osaka 565-0871, Japan
[e] Department of Radiology, Kinki Central Hospital of Mutual Aid Association of Public School Teachers, 3-1 Kurumazuka, Itami-city, Hyogo 664-8533, Japan

ARTICLE INFO

Article history:
Received 22 September 2009
Received in revised form 12 March 2010
Accepted 19 March 2010

Keywords:
Computed tomography (CT)
Volumetric CT
Small peripheral pulmonary adenocarcinoma
Ground-glass opacity
Pathological prognostic factors

ABSTRACT

Purpose: To evaluate a custom-developed software for analyzing malignant degrees of small peripheral adenocarcinomas on volumetric CT data compared to pathological prognostic factors.
Materials and methods: Forty-six adenocarcinomas with a diameter of 2 cm or less from 46 patients were included. The custom-developed software can calculate the volumetric rates of solid parts to whole nodules even though solid parts show a punctate distribution, and automatically classify nodules into the following six types according to the volumetric rates of solid parts: type 1, pure ground-glass opacity (GGO); type 2, semiconsolidation; type 3, small solid part with a GGO halo; type 4, mixed type with an area that consisted of GGO and solid parts which have air-bronchogram or show a punctate distribution; type 5, large solid part with a GGO halo; and type 6, pure solid type. The boundary between solid portion and GGO on CT was decided using two threshold selection methods for segmenting gray-scale images. A radiologist also examined two-dimensional rates of solid parts to total opacity (2D%solid) which was already confirmed with previous reports.
Results: There were good agreements between the classification determined by the software and radiologists (weighted kappa = 0.778–0.804). Multivariate logistic regression analyses showed that both 2D%solid and computer-automated classification were significantly useful in estimating lymphatic invasion ($p = 0.0007$, 0.0027), vascular invasion ($p = 0.003$, 0.012), and pleural invasion ($p = 0.021$, 0.025).
Conclusion: Using our custom-developed software, it is feasible to predict the pathological prognostic factors of small peripheral adenocarcinomas.

1. Introduction

Adenocarcinoma is the most common histopathologic subtype of lung cancer, and its incidence has been increasing [1,2]. Recent advances in CT scanning technology have enabled the detection of small pulmonary nodules, most of which are peripherally located adenocarcinoma. Such early detection using CT may alter the course of treatment of adenocarcinomas and subsequently improve the prognosis [3,4]. Although there is general consensus regarding the pathologic diagnosis of early pulmonary adenocarcinoma [5–8], the clinical and radiologic diagnosis of early adenocarcinoma with favorable prognosis remains controversial. Many reports [8,9] have demonstrated that the size of the central collapse/fibrosis and the percentage of the bronchioloalveolar carcinoma (BAC) component can be used as prognostic indicators for small lung adenocarcinomas. The BAC component is commonly detected on CT as ground-glass opacity (GGO); defined as a hazy increase in lung attenuation that does not obscure the underlying vascular markings [10]. However, there is no generally accepted method for measuring the area of GGO.

A new radiologic classification of small pulmonary adenocarcinoma on thoracic thin-section CT has already been proposed [11]. This classification, which is significantly associated with pathological prognostic factors, is based on the findings of thin-section CT

* Corresponding author at: Department of Radiology, Osaka University Graduate School of Medicine (the institution at which the work was performed), 2-2 Yamadaoka, Suita-city, Osaka 565-0871, Japan. Tel.: +81 6 879 3434; fax: +81 6 879 3439.
E-mail address: m-yanagawa@radiol.med.osaka-u.ac.jp (M. Yanagawa).

0169-5002/$ – see front matter © 2010 Elsevier Ireland Ltd. All rights reserved.
doi:10.1016/j.lungcan.2010.03.009

scans, such as the presence of solid and GGO parts, the distribution of solid parts, and the rate of solid parts to the whole nodule. However, because this classification can only be evaluated visually on CT, observers may differ in their assessment regarding the presence of solid and GGO parts. The purpose of the present study was to evaluate the ability of our custom-developed software to automatically analyze the malignant degree of small peripheral adenocarcinomas on quantitative volumetric CT data compared to pathological prognostic factors.

2. Materials and methods

2.1. Patients and diagnoses

The present study was approved by the institutional review board. Informed consent was waived for retrospective review of patient records and images. The study population consisted of consecutive patients who had undergone surgery at one hospital from January 2001 through July 2005 for primary pulmonary adenocarcinomas with a diameter of 2 cm or less. CT scans were performed in all patients before surgery. In all patients, the pulmonary nodules with a diameter of 2 cm or less in the longest diameter had areas with GGO and/or solid parts on CT, and were completely surrounded by the lung or visceral pleura at surgery. Patients who had previous adenocarcinomas in the lungs or other organs and who had undergone chemotherapy before surgery were excluded from the study. Moreover, patients were also excluded if their thin-section CT data was not available. Forty-six patients (22 men, 24 women; age range, 43–78 years; mean age, 61 years) were included in the present study.

The histopathologic diagnosis of all nodules was non-mucinous adenocarcinoma. On the basis of the histologic growth pattern, the adenocarcinomas were classified into the following three subtypes: localized BAC ($n = 16$), adenocarcinoma with BAC component ($n = 29$), and adenocarcinoma without BAC component ($n = 1$). The 16 cases of BAC included 3 cases associated with atypical adenomatous hyperplasia.

2.2. Acquisition of thin-section CT images

Chest CT scans were conducted using a 4-detector row LightSpeed QXi Scanner (General Electric Medical Systems, Milwaukee, WI, USA), an 8-detector row LightSpeed Ultra Scanner (GE Healthcare Technologies, Milwaukee, WI, USA), or a 4-detector row Aquilion V-detector Scanner (Toshiba Medical Systems, Tokyo, Japan). The parameters used for the scans depended on the indication: collimation was 0.5 or 1.25 mm, pitch was 0.625–1.5, the rotation time was 0.5–0.8 s per rotation, exposure parameters were 120 kV and 200 mA, and the field of view was 200 mm. All image data were reconstructed with a high spatial frequency algorithm at a 0.5- or 1.25-mm interval. All CT scans were displayed on a monitor at lung window settings (level, −700 Hounsfield units [HU]; width, 1200 HU).

2.3. Development of software

2.3.1. Definition of GGO, semiconsolidation, and solid component

Radiologic classifications of small pulmonary adenocarcinomas were classified into six subgroups (types 1–6) according to malignant degree of the tumor, and were in agreement with a previous report [11] (Table 1). Generally, opacity of peripheral adenocarcinomas on CT can be visually broken down into three parts, such as GGO, semiconsolidation, and solid part. GGO was defined as an area exhibiting a slight, homogeneous increase in density, which did not obscure underlying vascular markings. Semiconsolidation was defined as an area exhibiting an intermediate homogeneous increase in density, which did not obscure underlying vascular markings. The solid part was defined as an area of increased opacification that completely obscured underlying vascular markings. Prior to the present study, we determined threshold CT values between GGO and semiconsolidation and between semiconsolidation and solid parts in an additional six cases with adenocarcinomas, other than those in the present study, in order to automatically segment the three parts using our custom-developed software. By consensus, two radiologists assessed whether the tumor was GGO, semiconsolidation, or solid part from CT images of these additional six adenocarcinomas.

Two automatic threshold selection methods for segmenting gray-level images were used in the present study, 1: Method-1, Otsu's method [12], and 2: Method-2, Kittler's method [13]. Method-1 is a nonparametric and unsupervised method of automatic threshold selection for picture segmentation [12]. This simple method enables the division of gray images into two separate images through the selection of a threshold from gray-level histograms. Utilizing only the zeroth- and the first-order cumulative moments of the gray-level histogram, extending this method to multithreshold problems is straightforward. Method-2 is based on "minimum error thresh-holding" [13]. A computationally efficient solution to the problem of minimum error thresholding is derived under the assumption that both object and pixel gray-level values are normally distributed. The thresholds between GGO and semiconsolidation were −547 HU using Method-1 and −534 HU using Method-2; those between semiconsolidation and solid part were −291 HU using Method-1 and −188 HU using Method-2 (Figs. 1 and 2).

2.3.2. Decision of cut-off value of rate of solid part to total tumor (% solid) for the three-dimensional classification of tumors

According to radiologic classifications used in the present study (Table 1), the two-dimensional % solid (2D%solid) of type 3 or 4 was less than 50%, and 2D%solid of type 5 was 50% or more on transverse CT images [11]. In expanding the classifications on two-dimensional images to those on three-dimensional images, the cut-off value of three-dimensional % solid (3D%solid) between types 3 and 5 was 35.4% [$=(0.5)^{3/2} \times 100\%$].

In contrast, nodules from a previous experiment conducted using ten adenocarcinomas, different from those used in the present study, were classified based on visual assessment, as only

Table 1
Radiologic classifications of small pulmonary adenocarcinomas on CT images.

Classification	Radiologic Findings
Type 1	Pure GGO
Type 2	Semiconsolidation (an area of an intermediate homogeneous increase in density, which did not obscure underlying vascular markings)
Type 3	Small solid part with a GGO halo (an area that consisted of a solid part and a surrounding GGO halo; the area of solid part should be less than 50% on transverse CT image)
Type 4	Mixed type (an area that consisted of GGO and solid parts that have air-bronchogram or that show a punctate distribution; the area of solid part should be less than 50% on transverse CT image)
Type 5	Large solid part with a GGO halo (the area of solid part should be 50% or more on transverse CT image)
Type 6	Pure solid type (a nodule visually appeared to consist of only solid components)

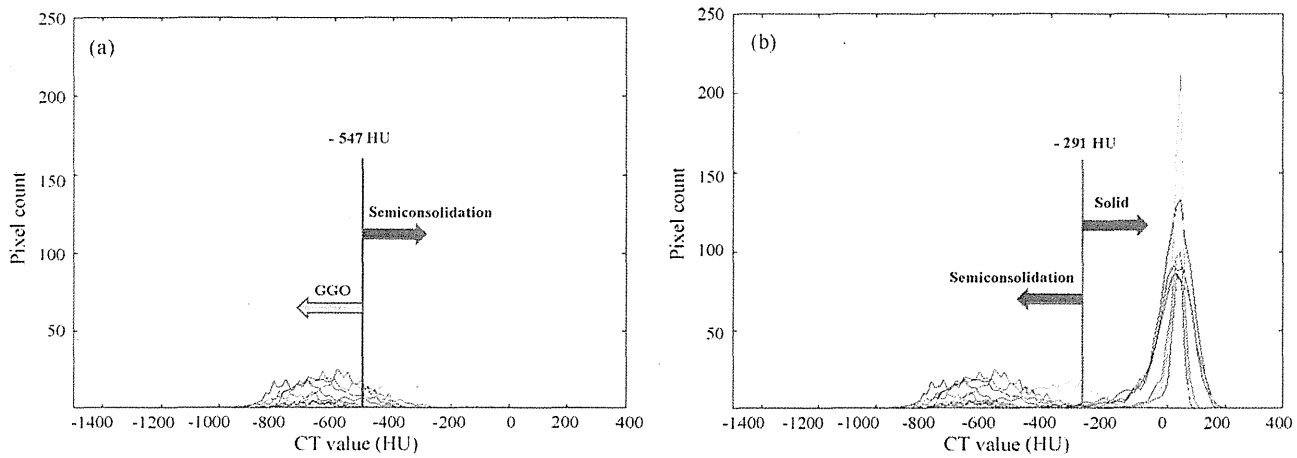

Fig. 1. (1) Threshold selection methods for segmenting gray-level images (Method-1, Otsu's method): the threshold between GGO and semiconsolidation. The gray-level histogram was generated using cases of type 1 (GGO) and 2 (semiconsolidation). The threshold (red line) between GGO and semiconsolidation was −547 HU using Method-1. (2) Threshold selection methods for segmenting gray-level images (Method-1, Otsu's method): the threshold between semiconsolidation and solid. The gray-level histogram was generated using cases of type 2 (semiconsolidation) and 6 (solid). The threshold (blue line) between semiconsolidation and solid was −291 HU using Method-1.

Table 2
Modified radiologic classifications on 3D-CT images.

Classification	Radiologic findings by Method-1 or Method-2
Type 1	Tumor with a CT value less than *x* HU.
Type 2	Tumor with a CT value from *x* HU to *y* HU.
Types 3–6	Tumor including a solid part with a CT value more than *y* HU.
Type 3	The volume rate of solid part should be less than 35.4%.
Type 4	The volume rate of solid part should be less than 35.4%. Solid parts have air-bronchogram or show a punctate distribution.
Type 5	The volume rate of solid part should be from 35.4 to 71.5%.
Type 6	The volume rate of solid part should be greater than 71.5%.

Method-1 (Otsu's method): $x = -547$, $y = -291$.
Method-2 (Kittler's method): $x = -534$, $y = -188$.

solid part (type 6). This experiment revealed that 2D%solid on transverse CT images calculated using Method-1 or Method-2 was equivalent to about 80%. Therefore, the cut-off value of 3D%solid between types 5 and 6 was 71.5% [$=(0.8)^{3/2} \times 100\%$]. The modified radiologic classifications on 3D images are summarized in Table 2.

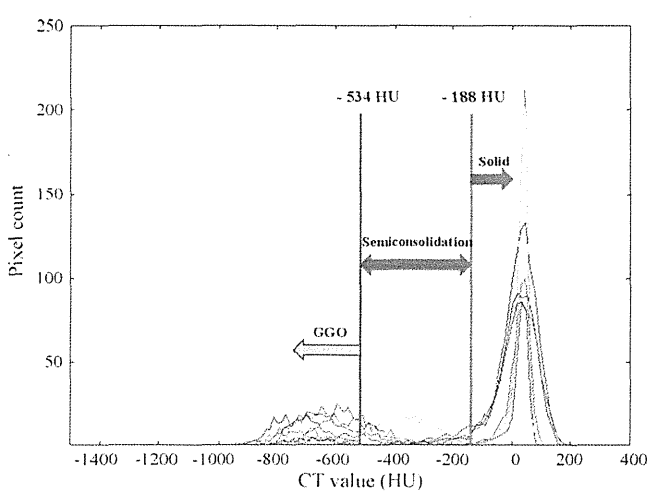

Fig. 2. Threshold selection methods for segmenting gray-level images (Method-2, Kittler's method): the thresholds among GGO, semiconsolidation and solid. Method-2 is based on "minimum error thresh-holding", which can decide more than two thresholds. The gray-level histogram was generated using cases of type 1 (GGO), 2 (semiconsolidation) and 6 (solid). The threshold (red line) between GGO and semiconsolidation was −534 HU and that (blue line) between semiconsolidation and solid was −188 HU using Method-2.

2.3.3. *Outline of custom-developed software*

Our software was developed using Microsoft Visual C++ 6.0 (Microsoft Corporation, Redmond, WA, USA) on a commercially available personal computer. It was a plug-in for the software used to segment the nodules on volumetric CT data, and used the following algorithm. First, by manually highlighting the boundary between the tumor and normal lung parenchyma on every CT slice, each volume of GGO, semiconsolidation, and solid part included in the highlighted area is automatically segmented. Next, the 3D%solid of the tumor is also automatically calculated. Finally, the tumors are automatically classified into the subgroups (types 1–6) (Fig. 3). Computer-automated classification according to malignant degree of the tumor on 3D-CT images is summarized in Fig. 4.

2.4. *Image analysis*

Three independent chest radiologists (with 8, 20 and 21 years of experience, respectively) visually classified tumors into the six subgroups (types 1–6) according to a previous report [11]. Final visual classification of the subgroup was decided by consensus.

The chest radiologist with 8 years of experience also manually examined 2D%solid on the maximum cross-section of the CT images directly on the monitor using a caliper, because the utility of a prognostic prediction using 2D%solid on CT images was already confirmed with previous reports [14].

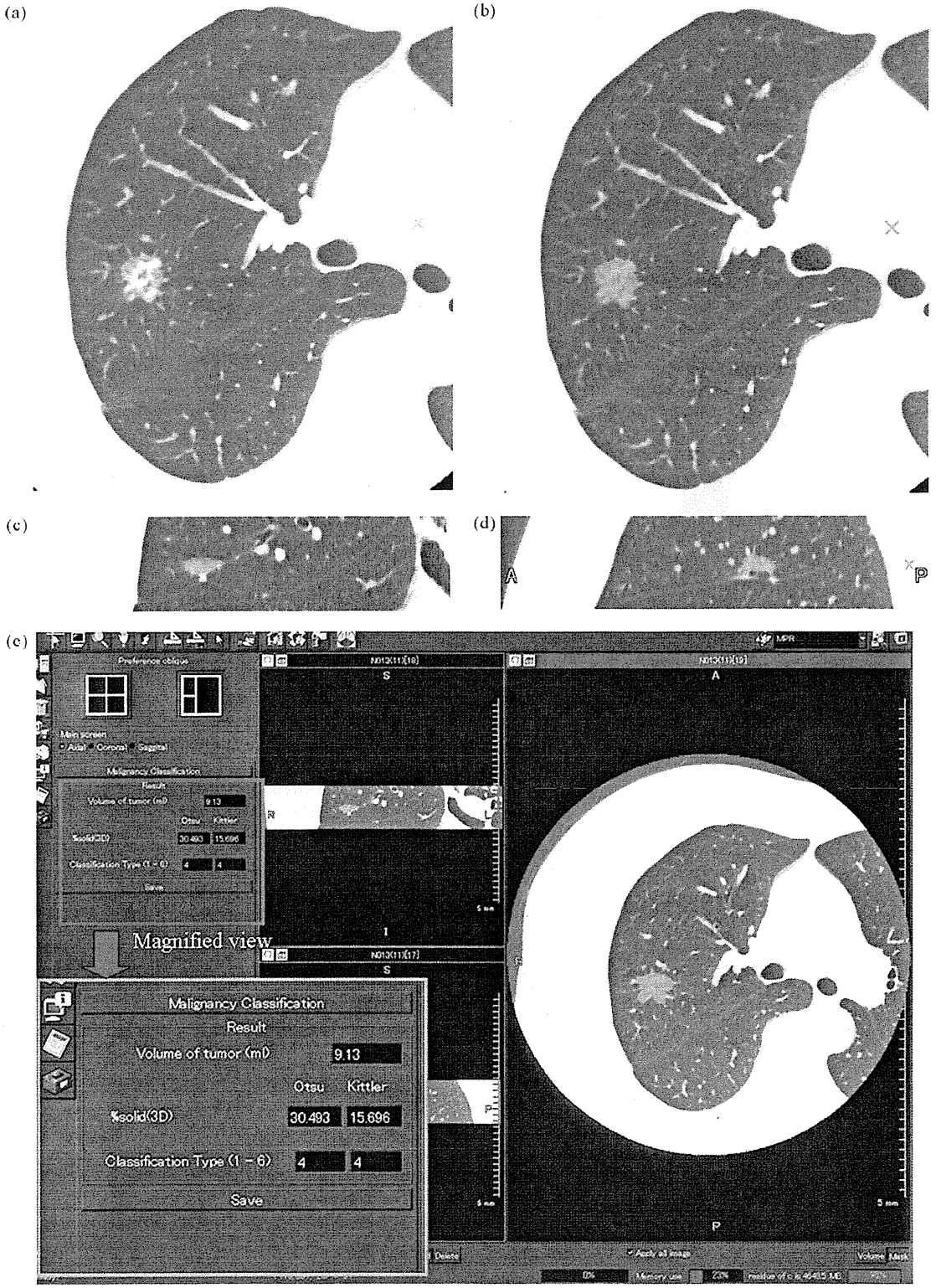

Fig. 3. A case of type 4 tumor in a 68-year-old woman. Axial CT image (a) shows a tumor with an area that consisted of GGO and solid parts. The green areas ((b) axial CT image, (c) coronal CT image, and (d) sagittal CT image) show an extracted tumor. Overall view of our software is shown by (e). Green frame is a magnified view of red frame. Our software indicates a tumor volume of 9.13 ml: 3D%solid using Method-1 is 30.493% and using Method-2 (Kittler's method) is 15.696%. Our software classified this tumor as type 4 (mixed type with an area that consisted of GGO and solid parts that have air-bronchogram or that show a punctate distribution).

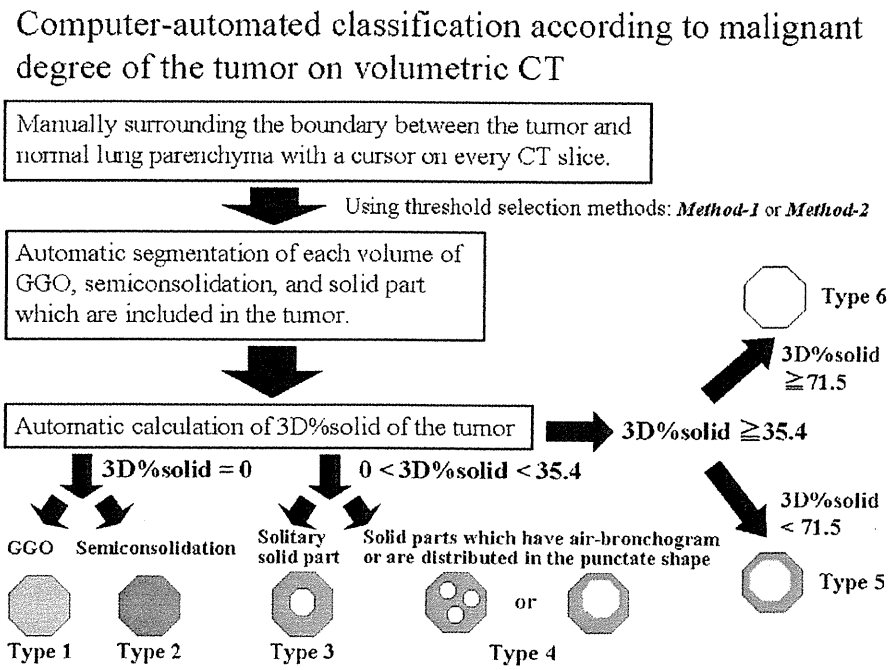

Fig. 4. Flow chart of computer-automated classification according to malignant degree of the tumor on volumetric CT.

This radiologist obtained the following information from the thin-slice CT images: the maximum dimension of tumor using a pulmonary window level setting (level, 600 HU; width, 1600 HU), the largest dimension of the perpendicular axis using a pulmonary window level setting, the maximum dimension of tumor using a mediastinal window level setting (level, 40 HU; width, 400 HU), and the largest dimension of the perpendicular axis using a mediastinal window level setting.

Highlighting of the boundary between the tumor and normal lung parenchyma using our software was conducted by two independent chest radiologists (4 and 8 years of experience). After discussion, the data from one experienced chest radiologist (the same radiologist who measured 2D%solid on CT) were used for analysis.

We evaluated three matters (vascular, lymphatic and pleural invasion) as pathological prognostic factors and examined the correlation of these three prognostic factors with the four explanatory variables: the visual classification of the subgroup; the classification using Method-1; the classification using Method-2 and manually measured 2D%solid.

2.5. Statistical analysis

Statistical analysis was performed using commercially available software (MedCalc Version 8.0.0.1, Frank Schoonjans, Mariakerke, Belgium). Inter-observer agreements of highlighted boundaries between tumors and normal lung parenchyma were assessed by Bland and Altman's method [15]. Agreements between visual and computer-automated classification were evaluated using the weighted κ statistic and classified as poor ($\kappa = 0.00$–0.20), fair ($\kappa = 0.21$–0.40), moderate ($\kappa = 0.41$–0.60), good ($\kappa = 0.61$–0.80), or excellent ($\kappa = 0.81$–1.00). Univariate and multivariate analyses were performed by logistic regression analysis. Forward and backward stepwise procedures were used to determine the combination of factors that were essential in predicting prognosis. A p value < 0.05 was considered to indicate significant difference.

3. Results

3.1. Inter-observer agreements

Inter-observer agreement between the two observers that manually highlighted the boundary between the tumor and normal lung parenchyma (mean bias ± 1.96 standard deviations) was −2.2 ± 9.5 mm (Fig. 5).

3.2. Agreements between visual classification and computer-automated classification

The visual classification by radiologists was as follows: type 1 (11/46 cases, 24%), type 2 (2/46, 4%), type 3 (4/46, 9%), type 4 (9/46, 20%), type 5 (13/46, 28%) and type 6 (7/46, 15%). The agreement between visual and computer-automated classification are shown in Table 3. Overall concordance between visual classification and classification using Method-1 was 32 (70%) of 46 tumors (weighted kappa = 0.799). Overall concordance between visual classification and the classification using Method-2 was 29 (63%) of 46 tumors (weighted kappa = 0.758).

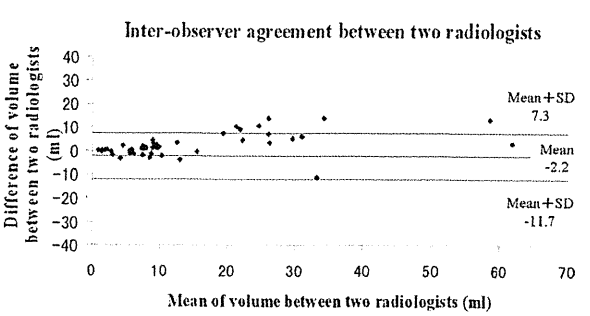

Fig. 5. Bland–Altman plot of inter-observer agreement between two radiologists.

Table 3
The agreement between visual and computer-automated classification (Method-1 or Method-2).

	Visual classification						Total
	Type 1	Type 2	Type 3	Type 4	Type 5	Type 6	
Method-1 (Otsu's method)							
Type 1	9	1	0	0	0	0	10
Type 2	1	0	0	0	0	0	1
Type 3	0	1	2	2	1	0	6
Type 4	1	0	1	5	0	0	7
Type 5	0	0	1	2	11	2	16
Type 6	0	0	0	0	1	5	6
Total	11	2	4	9	13	7	46
Weighted kappa value				0.799			
Method-2 (Kittler's method)							
Type 1	10	2	1	0	0	0	13
Type 2	0	0	0	1	0	0	1
Type 3	1	0	0	3	2	0	6
Type 4	0	0	3	5	1	0	9
Type 5	0	0	0	0	10	3	13
Type 6	0	0	0	0	0	4	4
Total	11	2	4	9	13	7	46
Weighted kappa value				0.758			

3.3. Manually measured 2D%solid on the maximum cross-section of CT

Manually measured 2D%solid (mean ± standard deviation) according to the visual classification is shown in Table 4. In the case of solid parts that have air-bronchogram or that show a punctate distribution (type 4), the radiologist made all possible efforts to measure the 2D%solid of tumors.

3.4. Pathologic characteristic according to classification of tumors

Pathologic characteristics in small pulmonary adenocarcinomas according to visual and computer-automated classification are summarized in Table 5. In both localized BAC ($n = 16$) and adenocarcinoma without BAC component ($n = 1$), there were no differences in distribution of pathologic characteristics among visual classification, classification using Method-1, and classification using Method-2. In adenocarcinoma with BAC component ($n = 29$), there were differences in distribution of pathologic characteristics among these three types of classifications. Univariate and multivariate logistic regression analyses are summarized in Tables 6.1 and 6.2. Univariate logistic regression analyses showed that classification using Method-1 and manually measured 2D%solid were both significantly useful in estimating all three pathological prognostic factors: lymphatic invasion ($p = 0.01$, 0.0007), vascular invasion ($p = 0.017$, 0.003) and pleural invasion ($p = 0.03$, 0.046). Multivariate logistic regression analyses also demonstrated that classification using Method-1 and manually measured 2D%solid were both significantly useful in estimating lymphatic invasion ($p = 0.0027$, 0.0007), vascular invasion ($p = 0.012$, 0.003) and pleural invasion ($p = 0.025$, 0.021).

Table 4
Manually measured two-dimensional % solid (2D%solid) according to visual classification.

Visual classification	2D%solid (mean ± SD)
Type 1 ($n = 11$)	0 ± 0
Type 2 ($n = 2$)	0 ± 0
Type 3 ($n = 4$)	0.182 ± 0.149
Type 4 ($n = 9$)	0.055 ± 0.072
Type 5 ($n = 13$)	0.444 ± 0.191
Type 6 ($n = 7$)	0.948 ± 0.135
Total ($n = 46$)	0.297 ± 0.354

4. Discussion

The present study demonstrates that our custom-developed software is useful for predicting lymphatic invasion, vascular invasion and pleural invasion in small peripheral adenocarcinomas. Even though pulmonary nodules show various CT patterns (GGO, semiconsolidation, part-solid, and pure solid) and have solid parts with a punctate distribution, predicting the pathological prognostic factors of them on CT images is feasible using our custom-developed software.

The prognosis of pulmonary adenocarcinoma with a larger area of GGO on thin-section CT images is much better than that of pulmonary adenocarcinoma of solid type on CT regardless of its maximal tumor dimension [4,16–21]. The extent of GGO is one of the most important prognostic factors. In fact, there were differences in distribution of pathologic characteristics among visual classification, classification using Method-1, and classification using Method-2 in adenocarcinomas with BAC component which is commonly detected on CT as GGO (Table 5). Many reports have demonstrated that manually measured 2D%solid on thin-section CT images was useful for predicting the prognostic outcome of small pulmonary adenocarcinomas [4,14,17–19,22–26]. However, the reproducibility of manual measurements is poor in evaluating small nodules [27,28]. Furthermore, malignant nodules do not always grow symmetrically, and tumors are often a heterogeneous mixture of GGO and solid parts. GGO can only be evaluated visually on CT images because there is no quantitative definition of GGO. Therefore, it is difficult to accurately measure the area of GGO and solid parts that have air-bronchogram or that show a punctate distribution, and considerable disagreement among radiologists on the diagnosis can arise.

Recent advances in diagnostic modalities have enabled the detection of increasingly smaller pulmonary adenocarcinomas with or without GGO in elderly patients. A suitable surgical approach that achieves the most benefit for these patients must be considered, and limited surgical resection has the benefit of preserving the postoperative quality of life without impairment of respiratory function [29]. Some reports [30,31] have suggested that

Table 5
Pathologic characteristics in small pulmonary adenocarcinomas according to visual and computer-automated classification.

Histopathologic diagnosis	Visual classification	Numbers of invasive tumors			Classification using Method-1 (Otsu)	Numbers of invasive tumors			Classification using Method-2 (Kittler)	Numbers of invasive tumors		
		LI	VI	PI		LI	VI	PI		LI	VI	PI
Localized BAC $n=16$	Type 1 ($n=9$)	0	1	0	Type 1 ($n=8$)	0	1	0	Type 1 ($n=11$)	0	1	0
	Type 2 ($n=2$)	0	0	0	Type 2 ($n=1$)	0	0	0	Type 2 ($n=1$)	0	0	0
	Type 3 ($n=1$)	0	0	0	Type 3 ($n=3$)	0	0	0	Type 3 ($n=2$)	0	0	0
	Type 4 ($n=3$)	0	0	0	Type 4 ($n=3$)	0	0	0	Type 4 ($n=1$)	0	0	0
	Type 5 ($n=1$)	0	0	0	Type 5 ($n=1$)	0	0	0	Type 5 ($n=1$)	0	0	0
	Type 6 ($n=0$)	0	0	0	Type 6 ($n=0$)	0	0	0	Type 6 ($n=0$)	0	0	0
Adenocarcinoma with BAC component $n=29$	Type 1 ($n=2$)	0	0	0	Type 1 ($n=2$)	0	0	0	Type 1 ($n=2$)	0	0	0
	Type 2 ($n=0$)	0	0	0	Type 2 ($n=0$)	0	0	0	Type 2 ($n=0$)	0	0	0
	Type 3 ($n=3$)	1	1	1	Type 3 ($n=3$)	1	0	0	Type 3 ($n=4$)	2	2	0
	Type 4 ($n=6$)	3	2	0	Type 4 ($n=4$)	1	1	0	Type 4 ($n=8$)	3	2	1
	Type 5 ($n=11$)	6	4	1	Type 5 ($n=14$)	9	6	1	Type 5 ($n=11$)	8	5	2
	Type 6 ($n=7$)	7	5	2	Type 6 ($n=6$)	6	5	3	Type 6 ($n=4$)	4	3	1
Adenocarcinoma without BAC component $n=1$	Type 1 ($n=0$)	0	0	0	Type 1 ($n=0$)	0	0	0	Type 1 ($n=0$)	0	0	0
	Type 2 ($n=0$)	0	0	0	Type 2 ($n=0$)	0	0	0	Type 2 ($n=0$)	0	0	0
	Type 3 ($n=0$)	0	0	0	Type 3 ($n=0$)	0	0	0	Type 3 ($n=0$)	0	0	0
	Type 4 ($n=0$)	0	0	0	Type 4 ($n=0$)	0	0	0	Type 4 ($n=0$)	0	0	0
	Type 5 ($n=1$)	1	0	0	Type 5 ($n=1$)	1	0	0	Type 5 ($n=1$)	1	0	0
	Type 6 ($n=0$)	0	0	0	Type 6 ($n=0$)	0	0	0	Type 6 ($n=0$)	0	0	0
Total $n=46$	Type 1 ($n=11$)	0	1	0	Type 1 ($n=10$)	0	1	0	Type 1 ($n=13$)	0	1	0
	Type 2 ($n=2$)	0	0	0	Type 2 ($n=1$)	0	0	0	Type 2 ($n=1$)	0	0	0
	Type 3 ($n=4$)	1	1	1	Type 3 ($n=6$)	1	0	0	Type 3 ($n=6$)	2	2	0
	Type 4 ($n=9$)	3	2	0	Type 4 ($n=7$)	1	1	0	Type 4 ($n=9$)	3	2	1
	Type 5 ($n=13$)	7	4	1	Type 5 ($n=16$)	10	6	1	Type 5 ($n=13$)	9	5	2
	Type 6 ($n=7$)	7	5	2	Type 6 ($n=6$)	6	5	3	Type 6 ($n=4$)	4	3	1

LI, lymphatic invasion; VI, vascular invasion; PI, pleural invasion.

Table 6.1
Univariate logistic regression analyses (forward and backward stepwise procedure).

Variable	Odds ratio	95% Confidence Interval	*p* Value
Lymphatic invasion			
Visual classification	3.99	1.6565–9.6293	0.002*
Classification using the Method-1 (Otsu's method)	12.36	1.7745–86.0956	0.01*
Classification using the Method-2 (Kittler's method)	3.7	1.6176–8.4713	0.002*
Manually measured two-dimensional % solid (2D%solid)	269.91	10.5143–6929.15	0.0007*
Vascular invasion			
Visual classification	1.83	1.0963–3.0457	0.02*
Classification using the Method-1 (Otsu's method)	2.31	1.1593–4.5964	0.017*
Classification using the Method-2 (Kittler's method)	1.73	1.0491–2.8598	0.03*
Manually measured two-dimensional % solid (2D%solid)	23.6	2.9398–189.5308	0.003*
Pleural invasion			
Visual classification	1.91	0.7553–4.8530	0.17
Classification using the Method-1 (Otsu's method)	13.58	1.2144–151.9337	0.03*
Classification using the Method-2 (Kittler's method)	2.52	0.7982–7.9872	0.11
Manually measured two-dimensional % solid (2D%solid)	9.5	1.0377–86.9719	0.046*

* Significant difference.

Table 6.2
Multivariate logistic regression analyses (forward and backward stepwise procedure).

Variable	Odds ratio	95% Confidence Interval	*p* Value
Lymphatic invasion			
Classification using the Method-1 (Otsu's method)	2.4	1.8249–17.7953	0.0027*
Manually measured two-dimensional % solid (2D%solid)	269.9	10.5143–17.7953	0.0007*
Vascular invasion			
Classification using the Method-1 (Otsu's method)	2.4	1.2176–4.8913	0.012*
Manually measured two-dimensional % solid (2D%solid)	23.6	2.9398–189.5308	0.003*
Pleural invasion			
Classification using the Method-1 (Otsu's method)	16.3	1.3991–189.9486	0.025*
Manually measured two-dimensional % solid (2D%solid)	54.6	1.08392–1621.0114	0.021*

* Significant difference.

segmental resection for small-sized lung cancer may be acceptable for patients with a tumor 2.0 cm or less in diameter (without nodal involvement), and that a peripherally located lung cancer with no lymph node metastasis might be the optimal indication for a more limited anatomic resection. Consequently, in current clinical settings, where limited surgical resection is desirable, the preoperative diagnosis of the invasiveness of a lung cancer becomes increasingly crucial for deciding the operative procedure. Therefore, in our study, in order to obtain an objective and quantitative assessment tool, we developed software that cannot only calculate 3D%solid of tumors including GGO area, but also automatically classify nodules according to the volumetric rates of the solid parts.

Automatic segmentation using the custom-developed software may enable high reproducibility during image assessment regardless of experience. In fact, commercially available software that can segment pulmonary nodules with GGO is already available. A previous study demonstrated that volumetric analysis is a reproducible and promising quantitative method using this commercially available software but that the correlation between the histological classification and the 3D%solid of tumors was no better when obtained using the software than when using manual measurements [32]. Although the automatic segmentation ability of our software can be improved, this software using Method-1 was as useful for predicting lymphatic invasion, vascular invasion and pleural invasion as the prognostic prediction using 2D%solid; in agreement with previous reports.

One of the important purposes of our study is to determine, as objectively as possible, the indication for limited surgical resection for lung adenocarcinomas by using our custom-developed software. Using visual classification, Suzuki et al. [11] demonstrated that types 1–4 were thought to be "minimally invasive" adenocarcinoma and that types 5 and 6 were considered to exhibit a "solid" course with higher possibility of lymph node metastases than types 1–4. If a tumor were classified as being types 1–4, the patient would be a candidate for limited surgical resection; whereas a type 5 or 6 tumor warrants major lung resection with systematic lymph node dissection necessarily. In classification using Method-1, useful for the prognostic prediction in the present study, types 5 and 6 tended to be more invasive than types 1–4 (Table 5): lymphatic invasion (types 1–4 vs. types 5 and 6), 2/24 (8%) vs. 16/22 (72%); vascular invasion, 2/24 (8%) vs. 11/22 (50%); and pleural invasion, 0/24 (0%) vs. 4/22 (18%).

However, six classifications proposed in our study are thought to remain important in order for the surgeon to plan for the management of peripheral lung cancer. In general, the progress of most small nodules that have been difficult to diagnose using CT has occurred over several years; with surgery only being indicated when tumors showed an increase in size on CT images. For instance, type 1 tumors (pure GGO) and type 2 tumors (semiconsolidation) show no solid parts on CT images. Most of the type 1 tumors are BAC, and are often indolent tumors. In contrast, type 2 tumors tend to be adenocarcinoma with pathologically invasive foci and grow in size. Concerning the surgical indications for tumors without solid parts, surgeons usually just monitor type 1 tumors without surgical interventions if the radiologic maximal tumor dimension is unchanged, and do not monitor type 2 tumors [11]. Thus, the clinical strategy depends on the six classifications, and the preoperative use of our custom-developed software will assist in determining a suitable operative method: limited surgical resection for tumors classified as types 1–4 and major lung resection for tumors classified as type 5 or 6.

There were several limitations in the present study. First, the number of patients was small for both the clinical evaluation and examination of the threshold of CT value between GGO and

semiconsolidation and between semiconsolidation and solid part. Subsequent analysis using a greater number of lung tumors is required. Second, in the image analysis, two independent readers were the minimum for this study with the current design. It might have been better for more independent readers to analyze image. Third, solid parts including vessels were calculated in our study, and may have introduced some bias into our results. In order to remove unnecessary vessels, this software will need to be upgraded by using "line filtering" [33], which enhances curvilinear structures, such as vessels and bronchi, in 3D medical images. Forth, although our software enabled automatic classification according to the malignant degree of small peripheral adenocarcinomas by automatically measuring 3D%solid of tumors, the initial highlighting of the boundary between the tumor and normal lung parenchyma was performed manually. The software is currently being upgraded to automate this procedure, which, in turn, may generate more objective results. Finally, our results should have been compared to the volumetric distribution of tumors in pathologic specimens, but postoperative collapse of the lung would have made accurate comparisons difficult.

In conclusion, predicting the pathological prognostic factors of small peripheral adenocarcinomas on three-dimensional CT images is feasible using our custom-developed software for evaluating their degree of malignancy. The application of this software will assist in deciding the future treatment strategies for small-sized adenocarcinoma of the lung following improvements in the filtering and automated segmentation feature.

Conflict of interest

No authors indicated potential conflicts of interest.

References

[1] Auerbach O, Garfinkel L. The changing pattern of the lung carcinoma. Cancer 1991;68:1973–7.
[2] Barsky SH, Cameron R, Osann KE, Tomita D, Holmes EC. Rising incidence of bronchioloalveolar lung carcinoma and its unique clinicopathologic features. Cancer 1994;73:1163–70.
[3] Henschke CI, McCauley DI, Yankelevitz DF, Naidich DP, McGuinness G, Miettinen OS, et al. Early lung cancer action project: overall design and findings from baseline screening. Lancet 1999;354:99–105.
[4] Aoki T, Tomoda Y, Watanabe H, Nakata H, kasai T, Hashimoto H, et al. Peripheral lung adenocarcinoma: correlation of thin-section CT findings with histologic prognostic factors and survival. Radiology 2001;220:803–9.
[5] Shimosato Y, Suzuki A, Hashimoto T, Nishiwaki Y, Kodama T, Yoneyama T, et al. Prognostic implications of fibrotic focus (scar) in small peripheral lung cancers. Am J Surg Pathol 1980;4:365–73.
[6] Noguchi M, Morikawa A, Kawasaki M, Matsuno Y, Yamada T, Hirohashi S, et al. Small adenocarcinoma of the lung. Histologic characteristics and prognosis. Cancer 1995;75:2844–52.
[7] Yokose T, Suzuki K, Nagai K, Nishiwaki Y, Sasaki S, Ochiai A. Favorable and unfavorable morphological prognostic factors in peripheral adenocarcinoma of the lung 3 cm or less in diameter. Lung Cancer 2000;29:179–88.
[8] Suzuki K, Yokose T, Yoshida J, Nishimura M, Takahashi K, Nagai K, et al. Prognostic significance of the size of central fibrosis in peripheral adenocarcinoma of the lung. Ann Thorac Surg 2000;69:893–7.
[9] Kurokawa T, Matsuno Y, Noguchi M, Mizuno S, Shimosato Y. Surgically curable "early" adenocarcinoma in the periphery of the lung. Am J Surg Pathol 1994;18:431–8.
[10] Austin JHM, Muller NL, Friedman PJ, Hansell DM, Naidich DP, Remy-Jardin M. Glossary of terms for CT of the lung: recommendations of the Nomenclature Committee of the Fleischner Society. Radiology 1996;200:327–31.
[11] Suzuki K, Kusumoto M, Watanabe S, Tsuchiya R, Asamura H. Radiologic classification of small adenocarcinoma of the lung: radiologic–pathologic correlation and its prognostic impact. Ann Thorac Surg 2006;81:413–20.
[12] Otsu N. A threshold selection method from gray-level histograms. IEEE Trans Syst Man Cybern 1979;SMC-9(1):62–6.
[13] Kittler J, Illingworth J. Minimum error thresholding. Pattern Recog 1986;19(1):41–7.
[14] Shimizu K, Yamada K, Saito H, Noda K, Nakayama H, Kameda Y, et al. Surgically curable peripheral lung carcinoma: correlation of thin-section CT findings with histologic prognostic factors and survival. Chest 2005;127:871–8.
[15] Bland JM, Altman DG. Statistical methods for assessing agreement between two methods of clinical measurement. Lancet 1986;1:307–10.
[16] Jang HJ, Lee KS, Kwon OJ, Rhee CH, Shim YM, Han J. Bronchioloalveolar carcinoma: focal area of ground-glass attenuation at thin-section CT as an early sign. Radiology 1996;199:485–8.
[17] Kodama K, Higashiyama M, Yokouchi H, Takami K, Kuriyama K, Mano M, et al. Prognostic value of ground-glass opacity found in small lung adenocarcinoma on high-resolution CT scanning. Lung Cancer 2001;33:17–25.
[18] Kim EA, Johkoh T, Lee KS, Han J, Fujimoto K, Sadohara J, et al. Quantification of ground glass opacity on high-resolution CT of small peripheral adenocarcinoma of the lung: pathologic and prognostic implications. AJR Am J Roentgenol 2001;177:1417–22.
[19] Ohde Y, Nagai K, Yoshida J, Nishimura M, Takahashi K, Suzuki K, et al. The proportion of consolidation to ground-glass opacity on high resolution CT is a good predictor for distinguishing the population of non-invasive peripheral adenocarcinoma. Lung Cancer 2003;42:303–10.
[20] Suzuki K, Asamura H, Kusumoto M, Kondo H, Tsuchiya R. "Early" peripheral lung cancer: prognostic significance of ground glass opacity on thin-section computed tomographic scan. Ann Thorac Surg 2002;74:1635–9.
[21] Yanagawa M, Kuriyama K, Kunitomi Y, Tomiyama N, Honda O, Sumikawa H, et al. One-dimensional quantitative evaluation of peripheral lung adenocarcinoma with or without ground-glass opacity on thin-section CT images using profile curves. Br J Radiol 2009;82(979):532–40.
[22] Kuriyama K, Seto M, Kasugai T, Higashiyama M, Kido S, Sawai Y, et al. Ground-glass opacity on thin-section CT: value in differentiating subtypes of adenocarcinoma of the lung. AJR Am J Roentgenol 1999;173:465–9.
[23] Takashima S, Maruyama Y, Hasegawa M, Yamada T, Honda T, Kadoya M, et al. Prognostic significance of high-resolution CT findings in small peripheral adenocarcinoma of the lung: a retrospective study on 64 patients. Lung Cancer 2002;36:289–95.
[24] Aoki T, Nakata H, Watanabe H, Nakamura K, Kasai T, Hashimoto H, et al. Evolution of peripheral lung adenocarcinomas: CT findings correlated with histology and tumor doubling time. AJR Am J Roentgenol 2000;174:763–8.
[25] Okada M, Nishio W, Sakamoto T, Uchino K, Tsubota N. Discrepancy of computed tomographic image between lung and mediastinal windows as a prognostic implication in small lung adenocarcinoma. Ann Thorac Surg 2003;76:1828–32.
[26] Matsuguma H, Nakahara R, Anraku M, Kondo T, Tsuura Y, Kamiyama Y, et al. Objective definition and measurement method of ground-glass opacity for planning limited resection in patients with clinical stage IA adenocarcinoma of the lung. Eur J Cardiothorac Surg 2004;25:1102–6.
[27] Revel MP, Bissery A, Bienvenu M, Aycard L, Lefort C, Frija G. Are two-dimensional CT measurements of small noncalcified pulmonary nodules reliable? Radiology 2004;231:453–8.
[28] Jennings SG, Winer-Muram HT, Tarver RD, Farber MO. Lung tumor growth: assessment with CT—comparison of diameter and cross-sectional area with volume measurements. Radiology 2004;231:866–71.
[29] Stair JM, Womble J, Schaefer RF, Read RC. Segmental pulmonary resection for cancer. Am J Surg 1985;150:659–64.
[30] Yoshikawa K, Tsubota N, Kodama K, Ayabe H, Taki T, Mori T. Prospective study of extended segmentectomy for small lung tumors: the final report. Ann Thorac Surg 2002;73:1055–8.
[31] Okada M, Nishio W, Sakamoto T, Uchino K, Yuki T, Nakagawa A, et al. Effect of tumor size on prognosis in patients with non-small cell lung cancer: the role of segmentectomy as a type of lesser resection. J Thorac Cardiovasc Surg 2005;129:87–93.
[32] Sumikawa H, Johkoh T, Nagareda T, Sekiguchi J, Matsuo K, Fujita Y, et al. Pulmonary adenocarcinomas with ground-glass attenuation on thin-section CT: quantification by three-dimensional image analyzing method. Eur J Radiol 2008;65(January (1)):104–11.
[33] Sato Y, Nakajima S, Shiraga N, Atsumi H, Yoshida S, Koller T, et al. Three-dimensional multi-scale line filter for segmentation and visualization of curvilinear structures in medical images. Med Image Anal 1998;2:143–68.

The Concept and Feasibility of EXPERT: Intelligent Armrest Using Robotics Technology

Tetsuya Goto, MD*
Kazuhiro Hongo, MD*
Takehiro Yako, MD*
Yosuke Hara, MD*
Jun Okamoto, DEng‡§
Kazutaka Toyoda, DEng‡
Masakatsu G. Fujie, DEng‡
Hiroshi Iseki, MD§

*Department of Neurosurgery, Shinshu University School of Medicine, Matsumoto, Japan; ‡Faculty of Science and Engineering, Waseda University, Tokyo, Japan; §Faculty of Advanced Techno-Surgery Institute of Advanced Biomedical Engineering and Science, Tokyo Women's Medical University, Tokyo, Japan

Correspondence:
Kazuhiro Hongo, MD,
Department of Neurosurgery,
Shinshu University School of Medicine,
3-1-1 Asahi,
Matsumoto 390-8621, Japan.
E-mail: khongo@shinshu-u.ac.jp

Received, June 13, 2012.
Accepted, August 9, 2012.

BACKGROUND: Continuous precise motions are required in microneurosurgery to provide high-quality surgical results. Stabilizing the surgeon's arm and reducing fatigue during surgery are expected to improve the precision of microsurgical procedures. We have developed an intelligent armrest, EXPERT, that follows the surgeon's hand and fixes at an adequate position automatically using robotics technology.

OBJECTIVE: To understand the feasibility of EXPERT by using the system in laboratory experiments and clinical situations.

METHODS: EXPERT has an arm holder and acts as a passive controlled robot with 5 degrees of freedom. The system has 3 modes: transfer, arm-holding, and arm-free mode, which are selected automatically. In the transfer mode, the arm holder follows the surgeon's arm. In the arm-holding mode, EXPERT supports the surgeon's arm weight by fixing the arm holder. The surgeon can move his/her arm away from the arm holder in the arm-free mode. The surgeon can change the position of armrest while looking through the microscope and can continue the microsurgical procedure while holding surgical instruments. Since 2010, EXPERT has been applied in 13 surgeries.

RESULTS: The EXPERT system decreased surgeon fatigue and reduced difficulty in performing surgical procedures. The EXPERT system markedly reduced surgeon hand tremor. There were no complications related to the use of this system.

CONCLUSION: EXPERT is a useful tool for holding the surgeon's arm comfortably and following the surgeon's arm automatically.

KEY WORDS: Movable armrest, Microneurosurgery, Robotics surgery, Surgeon supporting device

Neurosurgery 72:A39–A42, 2013 DOI: 10.1227/NEU.0b013e318271ee66 www.neurosurgery-online.com

In microneurosurgical procedures, continuous precise procedures are required to provide high-quality surgical results. Stabilizing the surgeon's arm with an armrest during surgery is expected to improve the precision of microsurgical procedures.[1] A freely movable armrest (FMA) was developed to support the surgeon's hand during surgery[2]; however, it has not been widely used because it requires continuous manual user interaction.[1,2] We have developed a new intelligent armrest using robotics technology. This system was designed so that the arm holder follows the surgeon's arm and fixes in the adequate position automatically. Here, we describe this system in detail and present preclinical and clinical results.

ABBREVIATION: FMA, freely movable armrest

METHODS

Concept of the Arm-Holding Device

We produced a prototype model to fulfill our requirements, which we called EXPERT (Figure 1). EXPERT consists of an arm holder, a holder support, and a base. The arm holder is made from the thermoplastic polymer Ortholen, which is widely used in prosthetic limbs. It has a curved shape and holds the surgeon's forearm. Three small electric magnets are set in the arm holder. A 6-axis force sensor is set between the arm holder and the holder support. The holder support has 5 degrees of freedom. No electric motors are used in the holder support. Each joint has springs and/or counterweights, electric brakes, and encoders. The base has 3 wheels to stand and move the EXPERT system. The system is attached to the operator's chair (Micro Chair, Mizuho Ikakogyo Co, Ltd, Tokyo, Japan) at the base; it is independent of the height adjustment of the chair but follows the forward/backward movement of the chair.

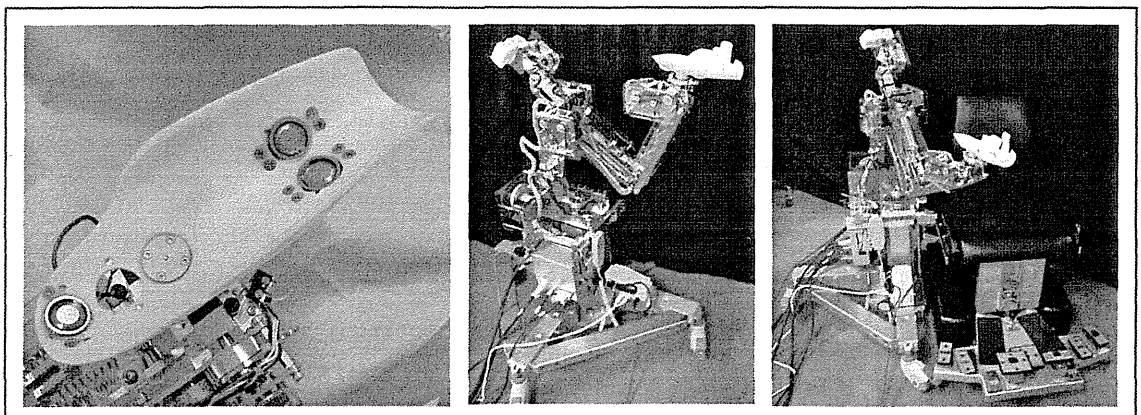

FIGURE 1. **Left,** *photograph of the arm holder made of Ortholen with 3 electromagnets installed.* **Center,** *photograph of EXPERT. The arm holder is indicated by the yellow circle; the holder support, by the green circle; and the base, by the red circle.* **Right,** *EXPERT is fixed to the operative chair. The holder support moves independently of the operative chair.*

EXPERT has 3 working modes: the transfer, arm-holding, and arm-free modes, which are converted automatically by analyzing the signals from 6-axis force sensor and the encoders in each joint. There is no need to press any buttons or switches to change modes. The surgeon wears a ferromagnetic wristband that connects to the electric magnets in the arm holder beneath sterile clothing. In the transfer mode, the electric brakes are released and electromagnets are active, so that the arm holder follows the surgeon's arm from below. The movement is achieved by the magnetic force between the surgeon's arm and the arm holder. The power required to move the arm holder is $<$ 50 N. Most of the power is transferred to the upper side by springs, and the system reduces the surgeon's arm weight in the transfer mode. The force to move horizontally is $<$ 50 N. In the arm-holding mode, the arm holder maintains the position by locking the electric brakes and supports the surgeon's arm weight. When the surgeon moves his/her arm away from the arm holder, eg, to change surgical instruments or to move the operating microscope, it is in the arm-free mode. The arm holder maintains its position by locking the electric brakes. When there is no arm on the arm holder and the unit is in transfer mode, the arm holder moves away from the patient.

Laboratory Experiment

Simulated microneurosurgery, involving suturing a thin piece of rubber, was used to examine the use of EXPERT. One quarter of a 10-mm circle was incised in thin pieces of rubber 4 cm in diameter. This circle was placed in a bowl at a depth of 60 mm. The conical working space was formed by plastics in the center of the bowl, which was 55 mm in diameter at the surface and a 10- to 20-mm ellipse at greater depths. Five sutures with 10-0 nylon were put in the incised rubber at even intervals using an operating microscope with conventional surgical instruments (Figure 2). EXPERT was set on the right side of the operator's chair. Six experienced neurosurgeons were registered as test candidates. Three of the 6 evaluating neurosurgeons (T.G., K.H., T.Y.) are included as authors; the others are colleagues in our department. They practiced the task and use of EXPERT adequately beforehand. The task was carried out once with and once without EXPERT. In each task, performance time to complete suturing was recorded, and each test candidate was asked to give 3 subjective evaluations regarding hand tremor, fatigue, and impression of maneuverability. Subjective evaluations were scored on a visual analog scale in which 1 is the minimum fatigue and the worst to perform and 100 is the maximum fatigue and the best to perform.

Statistical Analysis

The data were analyzed by paired t test. $P < .05$ was taken to indicate statistical significance.

RESULTS

All tasks were performed successfully without mechanical error of the EXPERT system. The performance time and subjective evaluation score are summarized in Figure 3. Four of 6 test candidates showed shorter performance time with EXPERT. The performance time was not different with and without the EXPERT for the remaining 2 test candidates. All 6 test candidates reported lower scores of fatigue when using EXPERT. The maneuverability score was higher with EXPERT. Recorded video showed that hand tremor of each test candidate was reduced and manipulation was more stable with EXPERT.

Clinical Use

Since March 2010, EXPERT has been clinically applied in 13 surgeries at Shinshu University Hospital. Before surgery, clinical application of EXPERT had been approved by the ethics committee of Shinshu University School of Medicine, and informed consent was obtained from all patients and their families. After the usual preparation of craniotomy and dura opening, EXPERT, covered with a sterile sheet, was introduced into the operative field. A surgeon performed the operation with routine microneurosurgical procedures supported by the EXPERT system (Figure 4). The surgeons did not always use EXPERT because rapid procedures without stringent accuracy requirements could

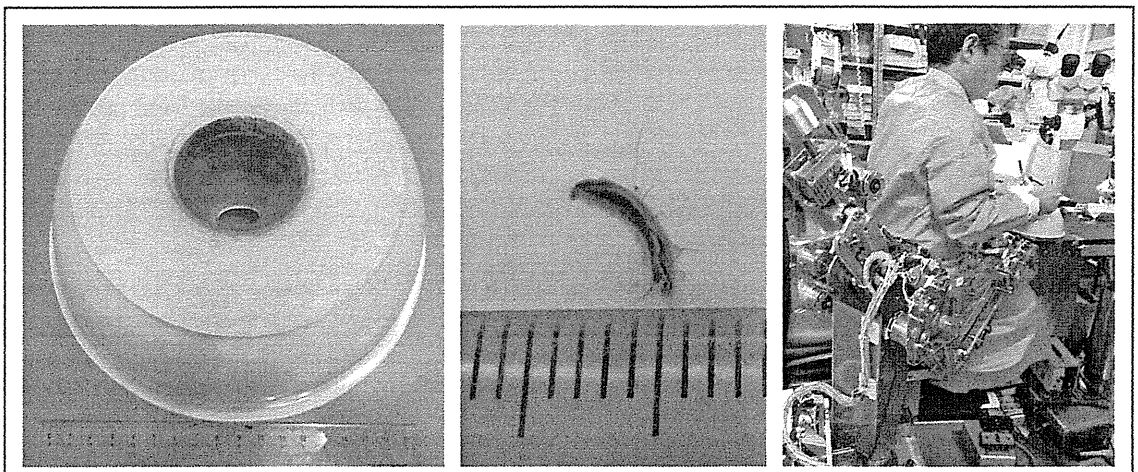

FIGURE 2. **Left,** *photograph of task field in laboratory experiment: 60-mm depth from surface, surface hole 55 mm in diameter, and elliptical deeper hole measuring 10 to 20 mm.* **Center,** *suture task. Five sutures were made with 10-0 nylon in a quarter-circle cut 10 mm in diameter on the thin piece of rubber* **Right,** *photograph of a laboratory experiment. An experienced neurosurgeon performed the task using EXPERT to support the right hand under an operating microscope.*

be performed easily without the system. There were no complications related to the use of EXPERT.

DISCUSSION

To provide high-quality surgical results, continuous precise motions are required in microneurosurgery. Precise movements can be achieved by maneuvering the surgical instruments with adequate stabilization of the surgeon's arm at the appropriate position. This has been achieved in conventional microneurosurgery by resting the surgeon's arm, hand, or finger on the patient's body or craniotomy edge and on the armrest of the surgical chair and a part of the head fixation frame.[3-10] The rigid, fixed-type armrest can be introduced easily but cannot completely cover the work space because many factors limit the surgeon's hand position. The brain surface cannot be touched or compressed by the surgeon's hand or arm. It is necessary to change the positions of brain spatula and self-retaining brain retractors frequently during surgery. The direction and angle of surgical instruments restricted by surrounding structures also limit the surgeon's hand position.

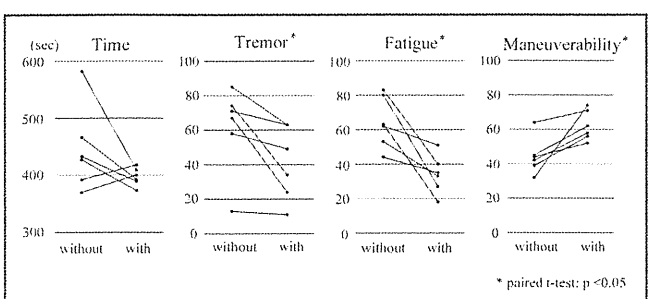

FIGURE 3. *Graph of the result. Fine lines indicate results for each test candidate without the EXPERT and with the EXPERT.* *P < .05.

An armrest with positions that can be changed as required is called an FMA and is considered effective. Ohta and Kuroiwa[2] developed the FMA (Smartarm, Mizuho Ikakogyo Co, Ltd, Tokyo, Japan) and reported its usefulness in neurosurgery. There is no doubt that the use of an FMA reduces operator fatigue and improves surgical maneuverability. We had also reported that the use of an FMA gave the operator a more relaxed posture and reduced both muscle stress and hand tremor compared with the use of a conventional armrest system.[1] Use of the FMA will reduce tremor when fine microsurgical movement is performed and thus will provide a good surgical result. Even if the surgeon can perform fine microsurgical movement without assistance of the FMA, more precise procedures can be performed with the FMA.

Despite its advantages for precise procedures, FMA-assisted surgery has not been widely adopted because its use is time-consuming and adjustment can be difficult. When the surgeon wishes to adjust the position of the FMA, eg, the Smartarm, it is necessary to put down the surgical instrument, push the button to change from locking to moving mode, adjust the position at which the arm is held, release the button to return from locking mode to moving mode, and retrieve the surgical instrument. These actions are time-consuming and troublesome. The optimal position of the surgeon's arm changes frequently, so real adjustment of the armrest to the optimal position may be impossible. The surgeon can identify the optimal position of the armrest while holding the surgical instrument in his/her hand and watching the operative view. When the position of armrest is incorrect, the adjustment action must be repeated. Therefore, the surgeon may continue

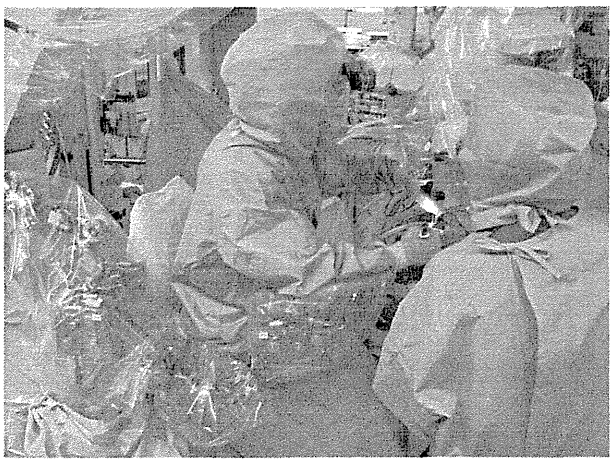

FIGURE 4. *Photographs of the operating room. The surgeon sits on the Micro Chair with the right hand supported by EXPERT.*

the procedure even if the position of the arm holder is not adequate.

EXPERT is classified as a type of FMA. However, EXPERT differs from an FMA in that it automatically follows the surgeon's arm. The surgeon can change the position of the armrest while using the microscope and can continue the microsurgical procedure while holding the surgical instrument. There is no need to push any buttons to convert between the lock and free modes. We believe that most disadvantages associated with the use of previous FMAs can be reduced by these functions of the EXPERT system.

Cost-effectiveness is also an important factor in widespread adoption. EXPERT is a surgeon support system and does not touch the patient. EXPERT is in the same equipment category as operating bed and operating chair and thus has no need for a clinical trial before commercial production. The potential commercial cost of EXPERT should be reasonably low.

Further improvement of EXPERT is necessary. The usefulness of EXPERT has been confirmed with only the right hand; however, using EXPERT with both hands may yield better results in microneurosurgery. The space occupied by EXPERT is also a problem because many surgical tools such as the operative microscope, navigation systems, drilling system, and coagulation system must be set near the surgeon. The base of EXPERT is large and heavy to prevent the system from falling or toppling over. Reducing the size of the EXPERT system while maintaining its functionality is a necessary future development. There is a tight feeling during transposition of the surgeon's arm because the supporting part must move automatically with the surgeon's hand motion.

The success of da Vinci surgical systems incited a dream to apply master-slave configured surgical robots in all surgical fields. Thus, the NeuRobot was developed for microneurosurgery.[11-13] From the experience with NeuRobot, we determined the difficulty of using surgical robots for microneurosurgery. Microneurosurgery is a fine art that only the human hand can produce. EXPERT provides support for a surgeon's art by allowing smooth and steady movement.

CONCLUSION

The intelligent armrest EXPERT held the surgeon's arm comfortably and followed the surgeon's arm automatically. EXPERT represents a useful tool for microneurosurgery. However, several modifications are required for commercial development of this system.

Disclosures

This project was supported by the Japanese Ministry of Education, Culture, Sports, Science and Technology Grant-in-Aid for Scientific Research No.19200043 (Dr Hongo). The arm holder was made by Arizonoseisakusyo Co, Ltd Japan. The holder supporting part and basal part was made by Hitachi JTE Co, Ltd, Japan. The surgical drape was made by Hogi Co, Ltd, Japan. There was no financial support from any companies. The main features of this system were already opened for patent in Japan No. 2008-151906 L0800004. Shinshu University and Waseda University preserve all rights without relevant company and individual persons. The authors have no personal financial or institutional interest in any of the drugs, materials, or devices described in this article.

REFERENCES

1. Yako T, Goto T, Hongo K. Usefulness and limitation of a freely movable armrest in microneurosurgery. *Int J Neurol Neurosurg.* 2009;1:185-190.
2. Ohta T, Kuroiwa T. Freely movable armrest for microneurosurgery: technical note. *Neurosurgery.* 2000;46(5):1259-1261.
3. Sugita K, Hirota T, Mizutani T. A newly designed multipurpose microneurosurgical head frame: technical note. *J Neurosurg.* 1978;48(4):656-657.
4. Kobayashi S, Sugita K, Matsuo K. An improved neurosurgical system: new operating table, chair, microscope and other instrumentation. *Neurosurg Rev.* 1984;7(2-3):75-80.
5. Gilsbach JM, Lutze T, Seeger W. Combined retractor and hand-rest system for neurosurgery. *Neurosurg Rev.* 1984;7(2-3):85-87.
6. Greenberg IM. Self-retaining retractor and handrest system for neurosurgery. *Neurosurgery.* 1981;8(2):205-208.
7. Tamaki N, Ehara K, Matsumoto S. The "thousand-hands Kannon" universal headframe: technical note. *J Neurosurg.* 1989;71(6):945-946.
8. Pritz MB, Hopkins JW. Armrest for STA-MCA bypass surgery. *Surg Neurol.* 1980; 14(5):370.
9. Klein F. Möller UNIVERSAL operation unit. *Neurosurg Rev.* 1984;7(2-3):99-102.
10. Yasargil MG, Vise WM, Bader DC. Technical adjuncts in neurosurgery. *Surg Neurol.* 1977;8(5):331-336.
11. Goto T, Hongo K, Kakizawa Y, et al. Clinical application of robotic telemanipulation system in neurosurgery: case report. *J Neurosurg.* 2003;99(6): 1082-1084.
12. Hongo K, Kobayashi S, Kakizawa Y, et al. NeuRobot: telecontrolled micromanipulator system for minimally invasive microneurosurgery: preliminary results. *Neurosurgery.* 2002;51(4):985-988.
13. Hongo K, Goto T, Miyahara T, Kakizawa Y, Koyama J, Tanaka Y. Telecontrolled micromanipulator system (NeuRobot) for minimally invasive neurosurgery. *Acta Neurochir Suppl.* 2006;98:63-66.

J Neurosurg 119:845–852, 2013

Phase II clinical study on intraoperative photodynamic therapy with talaporfin sodium and semiconductor laser in patients with malignant brain tumors

Clinical article

YOSHIHIRO MURAGAKI, M.D., PH.D.,[1,2] JIRO AKIMOTO, M.D., D.MED.SCI.,[3] TAKASHI MARUYAMA, M.D., PH.D.,[1,2] HIROSHI ISEKI, M.D., PH.D.,[1,2] SOKO IKUTA, PH.D.,[1] MASAYUKI NITTA, M.D., PH.D.,[1,2] KATSUYA MAEBAYASHI, M.D., PH.D.,[4] TAIICHI SAITO, M.D., PH.D.,[1,5] YOSHIKAZU OKADA, M.D., PH.D.,[2] SADAO KANEKO, M.D.,[6] AKIRA MATSUMURA, M.D., PH.D.,[7] TOSHIHIKO KUROIWA, M.D., PH.D.,[8] KATSUYUKI KARASAWA, M.D., PH.D.,[9] YOICHI NAKAZATO, M.D., PH.D.,[10] AND TAKAMASA KAYAMA, M.D., PH.D.[11]

[1]Faculty of Advanced Techno-Surgery, Institute of Advanced Biomedical Engineering and Science, and Departments of [2]Neurosurgery and [4]Radiation Oncology, Tokyo Women's Medical University, Tokyo; [3]Department of Neurosurgery, Tokyo Medical University, Tokyo; [5]Department of Neurosurgery, Hiroshima University, Hiroshima; [6]Kashiwaba Neurosurgical Hospital, Sapporo; [7]Department of Neurosurgery, University of Tsukuba, Ibaragi; [8]Department of Neurosurgery, Osaka Medical College, Osaka; [9]Department of Radiology, Tokyo Metropolitan Cancer and Infectious Diseases Center, Komagome Hospital, Tokyo; [10]Department of Human Pathology, Gunma University Graduate School of Medicine, Gunma; and [11]Department of Neurosurgery, Yamagata University, Yamagata, Japan

Object. The objective of the present study was to perform a prospective evaluation of the potential efficacy and safety of intraoperative photodynamic therapy (PDT) using talaporfin sodium and irradiation using a 664-nm semiconductor laser in patients with primary malignant parenchymal brain tumors.

Methods. In 27 patients with suspected newly diagnosed or recurrent primary malignant parenchymal brain tumors, a single intravenous injection of talaporfin sodium (40 mg/m^2) was administered 1 day before resection of the neoplasm. The next day after completion of the tumor removal, the residual lesion and/or resection cavity were irradiated using a 664-nm semiconductor laser with a radiation power density of 150 mW/cm^2 and a radiation energy density of 27 J/cm^2. The procedure was performed 22–27 hours after drug administration. The study cohort included 22 patients with a histopathologically confirmed diagnosis of primary malignant parenchymal brain tumor. Thirteen of these neoplasms (59.1%) were newly diagnosed glioblastomas multiforme (GBM).

Results. Among all 22 patients included in the study cohort, the 12-month overall survival (OS), 6-month progression-free survival (PFS), and 6-month local PFS rates after surgery and PDT were 95.5%, 91%, and 91%, respectively. Among patients with newly diagnosed GBMs, all these parameters were 100%. Side effects on the skin, which could be attributable to the administration of talaporfin sodium, were noted in 7.4% of patients and included rash (2 cases), blister (1 case), and erythema (1 case). Skin photosensitivity test results were relatively mild and fully disappeared within 15 days after administration of photosensitizer in all patients.

Conclusions. Intraoperative PDT using talaporfin sodium and a semiconductor laser may be considered as a potentially effective and sufficiently safe option for adjuvant management of primary malignant parenchymal brain tumors. The inclusion of intraoperative PDT in a combined treatment strategy may have a positive impact on OS and local tumor control, particularly in patients with newly diagnosed GBMs. Clinical trial registration no.: JMA-IIA00026 (https://dbcentre3.jmacct.med.or.jp/jmactr/App/JMACTRS06/JMACTRS06.aspx?seqno=862).
(http://thejns.org/doi/abs/10.3171/2013.7.JNS13415)

KEY WORDS • **malignant brain tumor** • **malignant glioma** • **oncology** • **photodynamic therapy** • **talaporfin sodium** • **outcome**

MALIGNANT brain tumors are characterized by invasive growth into adjacent normal neuronal tissue. Therefore, it is crucial that their man-

This article contains some figures that are displayed in color online but in black-and-white in the print edition.

Abbreviations used in this paper: GBM = glioblastoma multiforme; OS = overall survival; PDT = photodynamic therapy; PFS = progression-free survival; PS = performance status; 5-ALA = 5-aminolevulinic acid.

agement is directed not only to maximal possible resection (while ensuring preservation of the functionally important anatomical structures), but on suppressing the growth of the residual infiltrative tumor cells. Despite aggressive surgical removal followed by postoperative radiotherapy and chemotherapy, between 50% and 85% of WHO Grade IV gliomas recur locally.[9,16] This emphasizes the need for additional options to improve their growth control.

Photodynamic therapy (PDT) is a treatment method that involves administration of a photosensitizer that accumulates in tumor tissue and newly formed neoplastic vessels. During subsequent irradiation with a laser beam of a specific wavelength, the photosensitizer undergoes a photochemical reaction that produces singlet oxygen possessing strong oxidation properties that cause alteration of the cells. Because singlet oxygen has a short lifetime (0.04–4 μsec), the PDT-induced cell death is realized only locally in the areas irradiated by the laser beam.[2,7,8,15]

Talaporfin sodium (mono-L-aspartyl chlorine e6, or NPe6) is a relatively novel photosensitizer for PDT. Its administration in combination with a semiconductor laser has been approved in Japan for clinical use in cases of early stage lung cancer. Nonclinical pharmacological studies directed to its possible application for management of malignant brain tumors were initiated starting in 2001.[12–14] Experiments with glioblastoma cell lines demonstrated that such therapy induces mitochondrial apoptotic cell loss accompanied by tumor necrosis.[13,14] Our recent single-center pilot clinical study on the use of talaporfin sodium and a semiconductor laser in patients with malignant gliomas demonstrated promising results with regard to tumor response rates and treatment safety.[1] Therefore, the present open-label, prospective, multicenter clinical trial was initiated for evaluation of the potential efficacy and safety of such therapy. This study was the first investigator-initiated clinical trial in Japan that planned to assess the use of talaporfin sodium and a semiconductor laser for intraoperative PDT as part of a combined management of primary malignant parenchymal brain tumors.

Methods

Patients with suspected primary malignant parenchymal brain tumors, either newly diagnosed or recurrent, which according to preoperative neuroimaging corresponded to a WHO histopathological grade of III or IV,[11] were enrolled in this study. The recruitment of patients and analysis of treatment efficacy were mainly focused on newly diagnosed glioblastoma multiforme (GBM). The main inclusion criteria included agreement of the patient to provide written informed consent to participate in the study; age between 20 and 69 years at the time of informed consent; performance status (PS) score of 0, 1, 2, or 3 according to Eastern Cooperative Oncology Group PS scale (a PS score of 3 was accepted only when the score was attributable to neurological symptoms caused by the tumor); supratentorial location of the tumor not including neoplasms originating from the optic pathways and pituitary gland; absence of subarachnoid dissemination; and eligibility for aggressive resection of the lesion. The main exclusion criterion was a history of photosensitivity or porphyria.

Study Design

This prospective clinical trial was developed and carried out in 2 neurosurgical centers with well-established neurooncology programs, namely Tokyo Women's Medical University and Tokyo Medical University. An open-label, investigator-initiated clinical study was conducted in accordance with the Declaration of Helsinki. The research protocol was approved by the Pharmaceuticals and Medical Devices Agency of Japan as well as by the ethics committees and institutional review boards of both participating universities. A special review board was formed for central radiology assessment, evaluation of data related to treatment efficacy and safety, and handling of the enrolled cases and overall data management. Additionally, a pathology board was created for central review of the permanent formalin-fixed tissue specimens to determine the histopathological tumor type and grade. The 3-year study period was scheduled from March 21, 2009, to February 28, 2012. The clinical trial information for this study can be found at https://dbcentre3.jmacct.med.or.jp/jmactr/App/JMACTRS06/JMACTRS06.aspx?seqno=862.

Patients who were considered eligible for enrollment into study received a single intravenous injection of talaporfin sodium (Laserphyrin, Meiji Seika Pharma Co., Ltd.) in a dose of 40 mg/m^2 on an inpatient basis 1 day prior to undergoing the elective craniotomy. The next day, surgery was done, the neoplasm was resected, and irradiation of the resection cavity with a 664-nm semiconductor laser beam (Panasonic Healthcare Co., Ltd.), with a diameter of 1.5 cm, radiation power density of 150 mW/cm^2, and radiation energy density of 27 J/cm^2, was performed. Particular emphasis was put on irradiation of the areas at risk for recurrence, such as the genu of the corpus callosum.[9] If tumor resection was incomplete and the residual lesion was macroscopically identified, additional irradiation by the laser was applied at 1 to 3 sites with avoidance of overlap of the irradiation areas. In all cases laser irradiation was done 22–27 hours after administration of talaporfin sodium.

Postoperative Treatment and Follow-Up

Postoperatively all patients with newly diagnosed gliomas underwent fractionated radiotherapy (total dose 60 Gy) with concomitant and adjuvant chemotherapy using ACNU (in cases of WHO Grade III tumors) or temozolomide[18] (in cases of GBM). Patients with recurrent neoplasms were treated according to the preference of their doctors, taking into consideration the details of the primary management.

Adverse effects of treatment were graded according to the Common Terminology Criteria for Adverse Events version 3.0.[3] Follow-up examinations were performed every 2–3 months and included physical and neurological assessments with evaluation of PS score, blood and urine tests, and contrast-enhanced MRI. Tumor progression was defined as a 25% or greater increase in the volume of the contrast-enhanced lesion or the appearance of